Three-dimensional two-fluid modeling of a cylindrical fluidized bed and validation of the Maximum Entropy method to determine bubble properties

C. Sobrino*, A. Acosta-Iborra, M.A. Izquierdo-Barrientos, M. de Vega

Corresponding author: Tel +34 916248885. E-mail address: csobrino@ing.uc3m.es

Departamento de Ingeniería Térmica y de Fluidos, Universidad Carlos III de Madrid, ISE

Research Group, Avda. Universidad 30, 28911 Leganés, Madrid, Spain

Abstract

Diameter and velocity of bubbles from a three-dimensional two-fluid model simulation of a cylindrical fluidized bed are presented. Two methods for obtaining the bubble size and velocity are compared: i) estimation from the chord lengths and velocities of the detected bubbles using information from two virtual voidage probes (pierced bubble method) and ii) calculation from the bubble volume and velocity directly obtained from the instantaneous 3D voidage field (tomography method). The Maximum Entropy method (MaxEnt) is employed to convert probability density functions of chord lengths into the corresponding diameter distributions. The algorithm for the direct evaluation of the bubble volume and velocity, based on the tomography reconstruction of the 3D field, is explicitly explained and used to evaluate the results obtained from the virtual void probe signals. Results show a good agreement between the bubble sizes obtained using the MaxEnt treatment of the chord lengths and the directly obtained bubble sizes, which confirms the robustness of the MaxEnt method to infer bubble behavior in 3D bubbling beds. In particular, the mean bubble diameter obtained with the MaxEnt method applied to chord lengths was less than 4.5% different to the result from the tomography reconstruction. It was found that the bubble velocities obtained from virtual voidage probes are higher than the bubble velocities calculated with the tomography method, but the differences were not greater than 17% in the worst case. The probability density functions of bubble size and velocity obtained with the two methods were similar in terms of the location of the most probable values and the variation of the distribution with the distance to the distributor.

Keywords: Fluidized bed; Bubble size distribution; Bubble velocity; Maximum Entropy method; Two-fluid modeling.

1. Introduction

Fluidized beds are widely used in industrial processes involving mixing, drying or chemical reactions, because of their high heat and mass transfer efficiencies. Understanding the dynamics of these systems is a key issue to improve their performance and allow their proper scale-up from laboratory models. In particular, extracting relevant information of bubbles in bubbling fluidized beds is a matter of principal interest as bubble size and velocity, among

temporal frequency and spatial distribution of the bubbles in a bed, are relevant parameters affecting mixing and heat exchange [1].

There are many experimental and computational studies reported in the literature referring to bubble behavior in beds of small thickness, i.e. the so called pseudo two-dimensional (2D) beds, and in purely 2D beds [2,3,4,5,6,7,8,9]. These 2D configurations have the experimental advantage that they are optically accessible and they are not too computationally expensive to simulate. Referring to bubble size, imaging techniques in 2D beds allow the definition of a planar bubble contour, and the corresponding size is commonly represented by an area-equivalent bubble diameter defined as the diameter of a circle having the same area identified in the image [2]. In the same manner, in 2D simulated beds, bubbles are identified using the simulated voidage, and the equivalent volume bubble diameter is defined as the diameter of a circle with the same area as the area in which the simulated voidage is larger than a given threshold. Values for this threshold ranging from 0.7 to 0.85 have been reported in the literature [7,10,11]. In spite of the valuable information provided by 2D configurations, the most commonly used geometries in industry are three-dimensional (3D). However, 3D studies are rarely found in the literature as they still pose a challenge from the numerical point of view because of their high computational cost, as well as experimentally, because flow visualization and measurements are difficult to perform [12].

In 3D beds, tomography techniques such as electrical capacitance [13] or X-ray [14], are very promising methods since they utilize field measurements to quantify local property variations without interference of the fluidization process. While these techniques have proven their reliability in providing time averaged gas holdup [15,16], the definition of the bubbles is still challenging. In order to extract the bubble diameter or volume, a bubble defining parameter must be established. Even though there is no uniform method for separating the bubble and emulsion phases due to the significant differences between the various imaging techniques, usually a solid fraction value is used to define the boundary between the bubble phase and the emulsion phase [13]. Despite the tomography measurements can be of different nature, as well as the reconstruction techniques employed, the obtained result is generally a series of two dimensional sliced images through the investigated object. The obtained slices can then be placed together to form a three-dimensional temporal or spatial image [17] where bubbles are identified. Besides this bubble identification, complete definition of bubbles needs a reverse algorithm to determine their characteristic volume from the reconstructed 3D images, which is a task computationally expensive. Moreover, details of the customized algorithms for the volume determination are almost always lacking. In [13], it is stated that the individual bubbles are segmented from the data by using generally custom written algorithms so that individual bubbles can be identified, which can then be used to determine each bubble's center of mass, diameter as well as the overall bubble frequency, but no detail about this procedure has been found. Other drawbacks of tomography techniques are that the required experimental equipment is expensive, they have only been proven in relatively small 3D fluidized beds and they present difficulties in distinguishing between multiple overlapping bubbles [18] as well as high uncertainties associated with small bubbles [19]. Moreover, errors even when measuring well-defined phantom objects have been quantified between 4% and 10%, depending on the iterations of the off-line algorithm employed in a ECT tomography, or

6% to 25% using a simultaneous algebraic reconstruction technique (SART) in a X-ray tomography [17].

Whereas the use of intrusive probes in 3D beds presents the drawback of a possible interference in the process, they are competitive alternatives in industrial or pilot plants to provide relevant information of bubble characteristics because they are cheap and easily installed. Intrusive experimental techniques use one or more probes inserted into the fluidized bed. These probes can be capacitance sensors, optical sensors or pressure transducers [20,21,22,23]. The probe measures a property of the emulsion phase and when a bubble passes, the difference in the measured property provides local information of the traversing bubble. In order to identify the bubble, a threshold technique is needed. The measured magnitude is actually the chord length of the bubble which depends on the position, the trajectory of the piercing path and the velocity of the bubble passage, among other parameters. As a second step, a backward transform is necessary to infer the size of the bubbles from the measured chord lengths distributions. This determination of the bubble size is not straightforward and different methods have been considered in the literature to encompass the backward transform. Numerical, analytical, non-parametrical and maximum entropy (MaxEnt) backward transforms are presented in the literature and reviewed in [24]. Using a Monte Carlo simulation for the generation of ellipsoidal bubbles, Rüdisüli et al. [24] studied the relation between the measured chord length distribution of pierced bubbles in a bed and the overall bubble size distribution obtained by means of forward and backward transforms. It was showed that, for ellipsoidal bubbles, the MaxEnt method [25,26] is the most powerful and most accurate of all backward transforms.

Modeling of 3D fluidized beds can be used to provide instantaneous, whole-field information on the bubble behavior in geometries close to real ones, improving scale up advantages. In [27] a full 3D simulation of a cylindrical bubbling fluidized bed provided information on bubble sizes and velocities by means of porosity time series as measured by virtual voidage probes and these results were compared with experimental observations. More recently, Verma et al. [28] specified also the characteristic sizes of bubbles in a simulated 3D fluidized bed. In [28] the contours of bubbles were determined by visualizing 2D porosity plots and a time-average value of the equivalent bubble diameter was calculated assuming the area of a bubble defined by the 2D plot to be circular. Verma et al. [12], in a 3D two-fluid simulation of the bubble formation in a fluidized bed, calculated also the equivalent volume bubble diameter of a single detaching bubble. In that case, the assumption of bubble sphericity was evaluated by quantifying the shape of the bubble with the bubble shape factor, which was defined as the ratio of the maximum diameter in vertical direction to the maximum diameter in the horizontal direction.

It is clear from the above comments that whichever the technique employed (experiments or simulations) the way the bubble is defined and the corresponding size (diameter) calculation are not straightforward. In the present work, following the idea of [29], a virtual experiment of a fluidized bed carried out using CFD modeling is used to validate a measurement technique. Here, as a novelty, a 3D CFD simulation of a fluidized bed and its virtual optical probe signals are presented to validate the Maximum Entropy method for determining bubble properties. This analysis is carried out using the instantaneous whole-field of void fraction in a 3D bubbling

bed that is simulated with a two-fluid model. Two methods are used here for the characterization of bubbles. In one method, the bubble size distribution is directly obtained from the tomography reconstruction of the bubble contour, according to a threshold applied to the simulated 3D voidage. In the other method, the size distribution is inferred from the chord lengths of the bubbles that are detected using the voidage signals acquired at a set of points in the simulated bed. The MaxEnt method is used to convert the chord length distribution to the equivalent volume bubble diameter distribution in the bed. Bubble velocities are also calculated with the pierced bubble method and with the tomography method. These results are obtained at different distances to the distributor. In this way, the objective of the work is twofold. Firstly, to develop a two-fluid 3D simulation and describe the corresponding algorithm to identify and calculate the volume, equivalent volume diameter and velocity of bubbles, independently of any assumption of the bubble shape. A second objective of this work is to extend the validation the MaxEnt method when applied as a robust technique to extract the bubble size distribution from information acquired by means of intrusive probes that pierce geometrically complex and irregular bubbles obtained from a full 3D simulated bed.

2. Two-Fluid modeling

A standard bed column in bubbling regime was simulated to create physically realistic bubbles that can be used to compare the determination of bubble characteristics using pierced bubble and tomography methods.

2.1. Simulated 3D bed

The bed column was cylindrical, with 0.193 m internal diameter and 0.8 m height. The particles of the bed were of Geldart's B-type classification, with density of 2632.5 kg/m^3 and diameter 540 μm. The settled bed height was 0.22 m. Air was injected uniformly at the bottom of the bed to emulate a porous plate with high distributor to bed pressure ratio. The top of the bed was connected to the exterior air at atmospheric conditions. The minimum fluidization velocity of the bed was experimentally measured in a bed of similar characteristics resulting in a value of U_{mf} =0.4m/s [27]. To reach fully bubbling conditions, the superficial air velocity was set to U_g=0.57m/s. A sketch of the simulated bed is presented in Fig. 1. The fluidized bed geometrical and operational characteristics are summarized in Table 1.
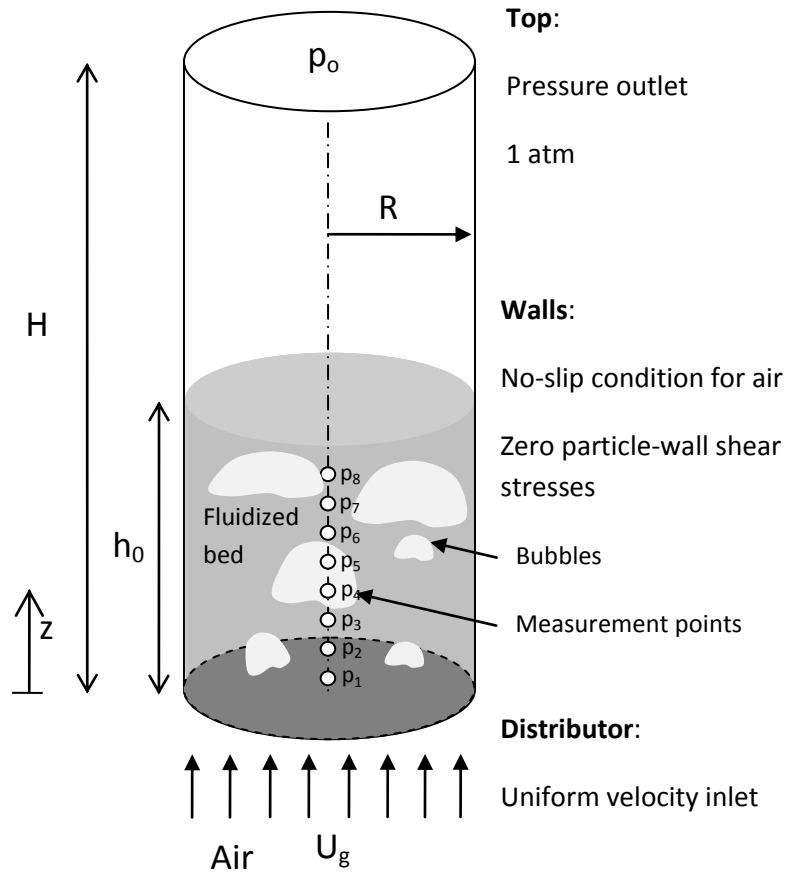
Fig. 1. Schematic representation of the simulated fluidized bed including the boundary conditions and virtual probes location.

Table 1 Main geometrical and operational characteristics of the fluidized bed.

Parameter	Value	Parameter	Value
R (m)	0.0965	ρ_p (kg/m³)	2632.5
H (m)	0.8	ρ_g (kg/m³)	1.225
h_0 (m)	0.22	μ_g (Pa·s)	1.789e-5
d_p (μm)	540	U_g (m/s)	0.57

The time evolution of the dense phase volume fraction was stored at eight different points along the bed axis (marked as p1 to p8 in Fig. 1) to mimic a set of dense phase probes (e.g. optical fiber or capacitance probes). The vertical separation between consecutive acquisition points was 1 cm starting with p1 at z =7 cm to the distributor and ending with p7 at z =14 cm. These virtual probes stored the solids volume fraction during a period of 60 seconds with a sampling frequency of 400 Hz. The first 7 seconds of the acquisition period were not considered to eliminate the start-up effects, so that the actual signal processing compressed 53 uninterrupted seconds of simulated time, ensuring with this that the results were statistically representative. The separation between probes and the sample frequency are the same as the ones used in [23] and [26].

2.2. Two-fluid governing equations

The gas-solid fluidized bed described in the previous section was simulated using an Eulerian description of both the gas and particle phases by means of a two-fluid model that resorts to the kinetic theory of granular flows [30]. This model makes use of the Eq. T2-1 to T2-4 described in Table 2 for the conservation of mass and momentum in both the gas phase (g) and particulate or solids phase (p), the last phase treated as a fluid with effective transport properties that interpenetrates the gas phase [31].

The mass and momentum equations are solved together with the differential Eq. T2-5 for the balance of granular temperature Θ [31], which is based on the kinetic theory of granular flows and provides the level of random fluctuation of particle velocity due to collisions.

Table 2 Governing equations of the two-fluid model.

Mass conservation equations

$$\frac{\partial}{\partial t}\left(\alpha_g \rho_g\right) + \nabla \cdot \left(\alpha_g \rho_g \mathbf{v}_g\right) = 0 \tag{T2-1}$$

$$\frac{\partial}{\partial t}\left(\alpha_p \rho_p\right) + \nabla \cdot \left(\alpha_p \rho_p \mathbf{v}_p\right) = 0 \tag{T2-2}$$

Momentum conservation equations

$$\frac{\partial}{\partial t}\left(\alpha_g \rho_g \mathbf{v}_g\right) + \nabla \cdot \left(\alpha_g \rho_g \mathbf{v}_g \mathbf{v}_g\right) = -\alpha_g \nabla p + \nabla \cdot \left(\alpha_g \boldsymbol{\tau_g}\right) - K_{gp}(\mathbf{v}_g - \mathbf{v}_p) + \alpha_g \rho_g \mathbf{g} \tag{T2-3}$$

$$\frac{\partial}{\partial t}\left(\alpha_p \rho_p \mathbf{v}_p\right) + \nabla \cdot \left(\alpha_p \rho_p \mathbf{v}_p \mathbf{v}_p\right) = -\alpha_p \nabla p - \nabla p_p + \nabla \cdot \left(\alpha_p \boldsymbol{\tau}_p\right) + K_{gp}(\mathbf{v}_g - \mathbf{v}_p) + \alpha_p \rho_p \mathbf{g} \tag{T2-4}$$

Granular temperature equation

$$\frac{3}{2}\left[\frac{\partial}{\partial t}\left(\rho_p \alpha_p \Theta\right) + \nabla \cdot \left(\rho_p \alpha_p \Theta \mathbf{v_p}\right)\right] = \left(-p_p \mathbf{I} + \boldsymbol{\tau}_p\right):\nabla \mathbf{v_p} + \nabla \cdot \left(k_\Theta \nabla \Theta\right) - \gamma_\Theta - 3K_{gp}\Theta \tag{T2-5}$$

In the governing equations it is implicit that $\alpha_g + \alpha_p = 1$. Besides the stress tensor of the momentum equations for any phase " i " is $\boldsymbol{\tau_i} = \mu_i(\nabla \mathbf{v}_i + \nabla \mathbf{v}_i{}^T) + \left(\lambda_i - \frac{2}{3} \mu_i \right)(\nabla \cdot \mathbf{v_i})\mathbf{I}$,

where the solids viscosity μ_p is computed with the collisional, kinematic and frictional viscosities $\mu_p = \mu_{p,col} + \mu_{p,kin} + \mu_{p,fr}$. Notice that the granular temperature Θ is required for the closure expressions of the viscosities of the solids phase μ_p and λ_p, the effective particle pressure p_p, the diffusion coefficient of granular temperature k_Θ and the collisional dissipation of energy γ_Θ. For the coefficient of drag between the gas and the particles, K_{gp}, the closure equation of Gidaspow et al. [32] has been chosen due to its robustness at the beginning of the simulation sequence, which commenced with air entering the distributor with the bed at rest and solids volume fraction $\alpha_{p.\max}$. Table 3 lists these and other closure models selected for the present simulation.

Table 3 Closure models selected for the simulation of the fluidized bed.

A.- Coefficient of drag between gas and particles [32]:

$$K_{gp} = \frac{3}{4} C_D \frac{\alpha_p \alpha_g \rho_g |\mathbf{v}_p - \mathbf{v}_g|}{d_p} \alpha_g^{-2.65} \quad \text{for } \alpha_g > 0.8 \tag{T3-1}$$

$$K_{gp} = 150 \frac{\alpha_p^2 \mu_g}{\alpha_g d_p^2} + 1.75 \frac{\alpha_g \rho_g |\mathbf{v}_p - \mathbf{v}_g|}{d_p} \quad \text{for } \alpha_g \leq 0.8 \tag{T3-2}$$

Where the drag coefficient is defined as:

$$C_D = \frac{24}{\alpha_g \operatorname{Re}_p} \left[1 + 0.15 \left(\alpha_g \operatorname{Re}_p \right)^{0.687} \right] \tag{T3-3}$$

With $\operatorname{Re}_p = \dfrac{\rho_g d_p |\mathbf{v}_p - \mathbf{v}_g|}{\mu_g}$ (T3-4)

B.- Solids pressure [33]:

$$p_p = \alpha_p \rho_p \Theta + 2\rho_p(1+e_{pp})\alpha_p{}^2 g_{0,pp}\Theta \tag{T3-5}$$

Where the radial distribution function is:

$$g_{0,pp} = \left[1 - \left(\frac{\alpha_p}{\alpha_{p,\max}}\right)^{1/3}\right]^{-1} \tag{T3-6}$$

C.- Solids stress tensor:

$$\boldsymbol{\tau}_p = \alpha_p \mu_p \left(\nabla \mathbf{v}_p + \nabla \mathbf{v}_p^{\mathrm{T}}\right) + \alpha_p \left(\lambda_p - \frac{2}{3}\mu_p\right)\nabla \cdot \mathbf{v}_p \, \mathbf{I} \tag{T3-7}$$

Where solid bulk viscosity is [33]:

$$\lambda_p = \frac{4}{3}\alpha_p \rho_p d_p g_{0,pp}(1+e_{pp})\left(\frac{\Theta}{\pi}\right)^{1/2} \tag{T3-8}$$

and solid shear viscosity is

$$\mu_p = \mu_{p,col} + \mu_{p,fr} + \mu_{p,kin} \tag{T3-9}$$

which is composed of a kinetic viscosity [32]

$$\mu_{p,kin} = \frac{10\rho_p d_p \sqrt{\Theta\pi}}{96\alpha_p\left(1+e_{pp}\right)g_{0pp}}\left[1 + \frac{4}{5}g_{0pp}\alpha_p\left(1+e_{pp}\right)\right]^2 \tag{T3-10}$$

a collisional viscosity [32]

$$\mu_{p,col} = \frac{4}{5}\alpha_p \rho_p d_p g_{0,pp}(1+e_{pp})\left(\frac{\Theta}{\pi}\right)^{1/2} \tag{T3-11}$$

and a frictional viscosity [34]

$$\mu_{p,fr} = \frac{p_p \sin\phi}{2\sqrt{I_{2D}}}$$ (T3-12)

where ϕ is the angle of internal friction, and I_{2D} is the second invariant of the deviatory stress tensor.

D.- Diffusion coefficient of granular temperature [32]:

$$k_\Theta = \frac{150\rho_p d_p \sqrt{\Theta\pi}}{384(1+e_{pp})g_{0pp}}\left[1+\frac{6}{5}\alpha_p g_{0pp}(1+e_{pp})\right]^2$$
$$+2\rho_p d_p \alpha_p^{\ 2} g_{0pp}(1+e_{pp})\sqrt{\frac{\Theta}{\pi}}$$ (T3-13)

E.- Collisional dissipation of energy [33]:

$$\gamma_\Theta = \frac{12(1-e_{pp}^{\ 2})g_{0,pp}}{d_p\sqrt{\pi}}\rho_p \alpha_p^{\ 2}\Theta^{3/2}$$ (T3-14)

2.3. Boundary conditions

The governing equations described in the previous section require the definition of a set of boundary conditions, as shown in Fig. 1. At the base of the cylinder, air at constant velocity U_g (Table 1) is uniformly injected into the fluidized bed. Particles are not allowed to cross the bottom of the cylinder. The top of the cylinder is assumed to have a constant static pressure of one atmosphere, since it is open to the exterior air. A no-slip condition for the gas flow was imposed at the lateral wall of the cylinder. For the dense phase flow, this condition is relaxed to no-penetration with negligible shear stresses at the lateral walls, since, in this kind of bed configuration, particles are well fluidized and rarely get attached to the wall. Hence, in the present cylindrical bed, the effects of the particle-wall shear stresses on the interior of the bed volume will be neglected. Besides, an imposition of other boundary conditions for the particle phase such as no-slip or partial-slip conditions would require, to be properly imposed, a highly refined mesh near the lateral walls that is impracticable for the present 3D simulation.

2.4 Numerical solution

The commercial CFD software ANSYS Fluent v12 was used for the solution of the system of equations of Tables 2 and 3 in a 3-D domain comprising all the interior volume of the cylinder where the fluidized bed is allocated. Table 4 collects the main simulation parameters. The 3D

domain was discretized with a boundary-fitted mesh of 28800 hexahedral cells and 30805 nodes. The gas and solids governing equations, in their transient and fully 3D form, were solved with an implicit finite volume technique (phase coupled SIMPLE) based on an iterative pressure correction [35]. Due to the great complexity and number of equations involved, a larger amount of cells would lead to an inadmissible time of computation. However, to improve the spatial and temporal resolution of the solution, second order discretization in space and time was selected. After a sensitivity analysis of the solution, the chosen time step was equal to 2.5e-4 seconds with 40 iterations per time step, together with an algebraic multigrid methodology for the solution of the implicit system of equations [36]. An effective value of the coefficient of restitution $e_{pp} = 0.9$ was chosen to take into account not only the dissipation of kinetic energy due to inelastic deformation of particles but also due to frictional losses [37].

Table 4 Main parameters selected for the simulation.

Parameter	Value	Parameter	Value
e_{pp} ( )	0.9	g (m/s^2)	9.81
$\alpha_{p,\max}$ ( )	0.555	Δt (s)	2.5e-4
ϕ (degree)	30	N_i	40

3. Data processing

3.1. Direct computation of bubble volume, diameter and velocity from simulation

One of the advantages of the use of simulations for analyzing the behavior of a 3D bubbling bed is, in principle, the unrestricted availability of data concerning the spatial distribution and time evolution of the gas and particulate phases. In particular, the 3D fields of solids volume fraction from two-fluid model simulations can be utilized to directly obtain relevant bubble parameters such as volume and velocity. Fig. 2 shows an example of bubbles rising in the simulated fluidized bed. The external form of the bubbles is qualitatively revealed in the figure by representing the iso-surfaces of solids volume fraction.
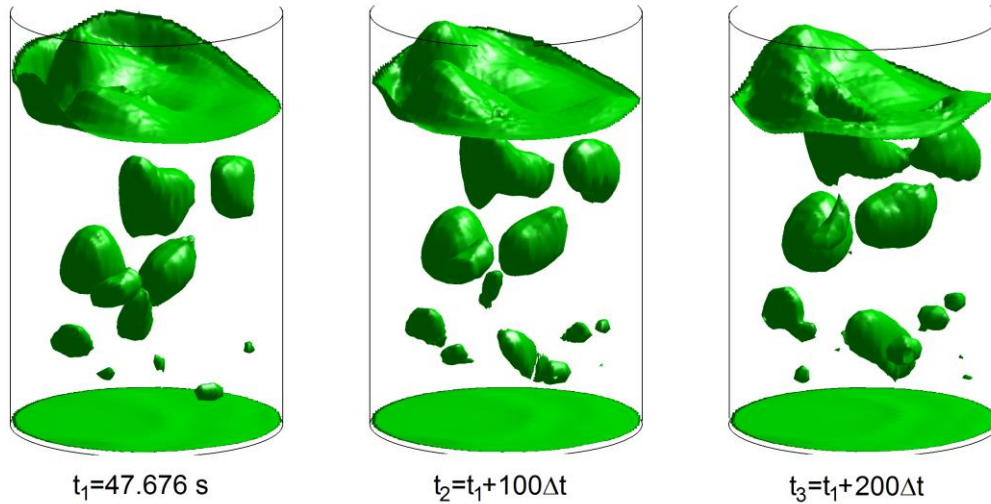
t_1=47.676 s t_2=t_1+100Δt t_3=t_1+200Δt

Fig. 2. Snapshots of isocontours for α_p=0.3 showing the 3D bubbles obtained from the two-fluid simulation at three sequential time instants.

However, the quantitative evaluation of the bubble size and velocity is not trivial because elaborate bubble recognition and tracking algorithms, working over the three spatial dimensions jointly with the time evolution, are needed. To circumvent these difficulties, a simple tomography reconstruction for the direct extraction of the 3D volume and velocity of bubbles is followed in this work as described in the steps below. Here, the word 'tomography' has been borrowed from the experimental terminology to denote the general process of 3D analysis using 2D information taken at different sections in a volume. The procedure, outlined in Fig. 3, is described through the following steps.

Step-1. Sectioning of the instantaneous 3D domain by horizontal planes. As mentioned in section 2, the instantaneous 3D fields of solids volume fraction from the fluidized bed simulations are saved at a rate of 400Hz. Each of these 3D fields is analyzed by means of horizontal sections that cut the whole bed volume. The vertical position of the horizontal sections coincides with the vertical position of the nodes of the mesh for the solids volume fraction. This yields a separation between consecutive sections of about 3mm near the distributor and 5 mm close to the bed surface, since the size of the mesh cells employed in the present study progressively grows with the distance to the distributor.

Step-2. Bubble contours detection in each horizontal section. Bubbles are detected in every horizontal section of Step-1 as conventionally done for 2D simulations (e.g. [5,7]). This requires the calculation of bubble contours using a threshold value $\alpha_{p,th}$ for the solids volume fraction.

Following previous works, an intermediate value $\alpha_{p,th} = 0.3$ is chosen for the bubble threshold [7,27]. For consistence, this threshold is equal to the one used for the calculation of the bubble chord length described in section 3.2. A region of solids volume fraction smaller than the threshold defines the interior area of a bubble sectioned by the horizontal plane (bubble section area). A bed section can cut multiple bubbles and the interior area and geometrical centroid are individually calculated for each of the resulting bubble sections.

Step-3. Stacking of bubble contours and 3D bubble identification. By stacking in order all the sections from an instantaneous 3D field, complete bubble contours are reconstructed. In order to do that, bubble contours pertaining to two consecutive sections are compared and assigned to a single bubble if the centroid of a bubble contour in a given section lays within the area delimited by the bubble contour in the next consecutive section, otherwise the two bubble contours are considered as sections pertaining to different bubbles. This comparison is performed for every pair of consecutive horizontal sections, starting from the lowest horizontal section of the bed (i.e. close to the distributor) to the highest section (just below the bed surface). However, the operation is repeated in inverse direction, i.e. from the higher section to the lowest one, so that confusion is avoided arising from deformed bubbles that can be sectioned more than once by a horizontal plane. The result of applying this staking procedure is the identification of several individual 3D bubbles pertaining to a time instant of the simulation, each bubble being described by a set of horizontal bubble contours as exemplified in Fig. 3.

Step-4. Calculation of 3D bubble parameters. For each of the 3D bubbles captured in Step-3, the bubble volume V_b is calculated by accumulating the product of the bubble section area and section thickness for the complete set of horizontal contours forming the bubble. The thickness of a given bubble section is defined as the mid distance between the sectional plane above the bubble section and the sectional plane below the bubble section. Higher order approximations of the bubble volume can be used but are not considered here for simplicity. The volume equivalent volume bubble diameter is then the diameter of a sphere whose volume equals the bubble volume calculated in this step, i.e. $D_v = \left(6V_b / \pi\right)^{1/3}$. Similarly, the bubble centroid is calculated with the centroids of each horizontal contour weighted with the bubble section area times the section thickness and divided by the bubble volume. Other parameters can be extracted such as the bubble surface area, aspect ratios, etc.

Step-5. Bubble tracking and calculation of its centroid velocity. After repeating Step-1 to 4 for every time instant exported from the simulation, the bubble displacement between consecutive time instants is obtained by comparing the centroid position of a bubble in a time instant, with the centroid positions of the bubbles in the next time instant. Two bubbles pertaining to two consecutive time instants are considered the same bubble if the module of the distance between their centroids is less than a tracking coefficient Ψ multiplying the mean value of their respective equivalent volume diameters. If for a bubble in a given time instant, more than one bubble of the next time instant complies with this criterion, the closest bubble is selected for the matching. A value Ψ =1.0 was selected for the results presented in this work, which was sufficient to ensure that only a single matching appeared for each bubble. Finally, the bubble velocity along any spatial direction is computed as the displacement of the bubble centroid in that direction divided by the time step between data frames. Again, higher order velocity estimations may be possible if bubbles are tracked over more than two consecutive time instants.
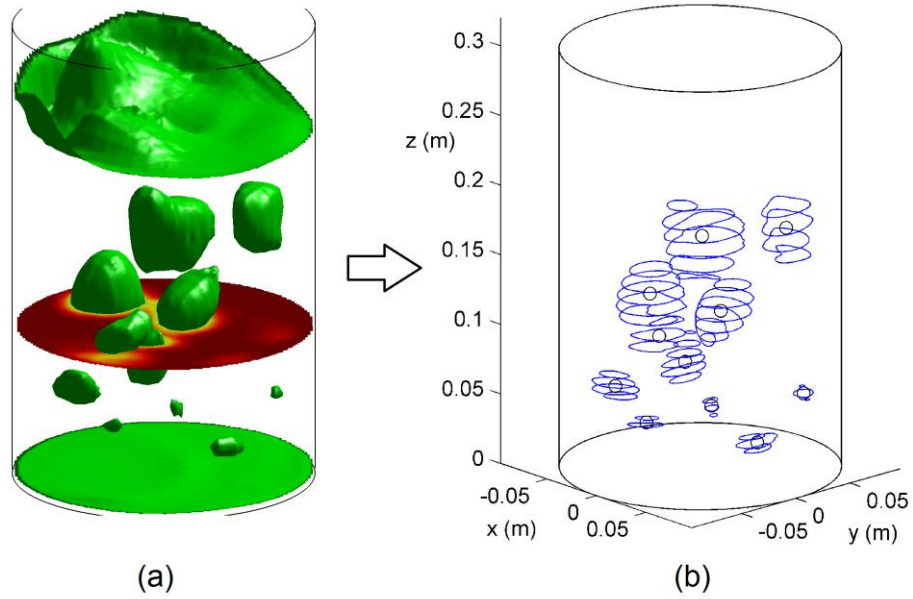
Fig.3. Tomographic identification and reconstruction of bubbles: (a) determination of sectioned bubble contours by horizontally sectioning the simulated field of solids volume fraction in the bed and (b) reconstruction of 3D bubbles by matching and pilling up the sectioned bubble contours. The small circle in each bubble denotes its centroid.

3.2. Estimation of bubble chord length and velocity from virtual probes

Bubble chord lengths and bubble velocities were calculated in the present work using the solids volume fraction signals collected from the series of virtual probes located at the seven different positions along the bed height shown in Fig. 1, with an axial separation of 1 cm. For the detection of bubbles it is considered that a bubble passage is occurring when the solids volume fraction falls below a threshold value equal to $\alpha_{p,th}$ =0.3. Fig. 4 shows the time evolution of the solids volume fraction obtained from the simulation at axial distances z=8cm and z =9 cm. The bubbles detected are marked with a circle placed at their lowest value of volume fraction. As the signals from two adjacent virtual probes are needed for the velocity determination, only bubbles detected by both probes are considered.
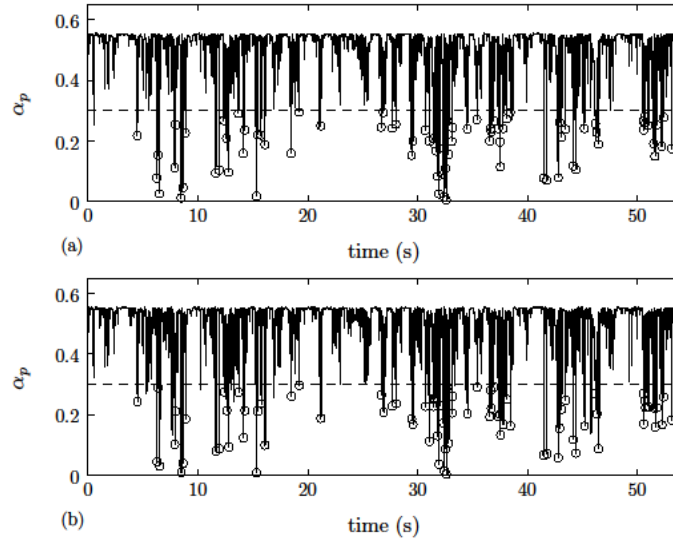
Fig. 4. Solids volume fraction at the bed axis and axial distance z =8 cm (a) and z =9 cm (b). The solids volume fraction threshold $\alpha_{p,th}$ =0.3 is indicated with a dashed line and bubbles detected are marked with a circle.

Fig. 5 shows an example of the calculation of bubble velocity and chord length for a bubble detected at the bed axis by the two adjacent virtual probes (i.e. lower and upper probes). Once a bubble has been detected, the bubble passage time is estimated as the local period of time during which the solids volume fraction signal falls below the threshold value. This passage time calculated with the lower or the upper probe is demarcated by crosses in Fig. 5. The rise velocity of a bubble is estimated by dividing the vertical separation between measurement points (1 cm) by the time taken by the bubble to travel from one point to the other. This time has been calculated by subtracting the central point of the bubble passage time of the upper probe to that of the lower probe. Then, the bubble chord length is calculated multiplying the bubble rise velocity by the bubble passage time. As in the work by Acosta-Iborra et al. [27], the bubble passage time determined with the lower probe signal is chosen for this chord length calculation. Of all the measured chord lengths, those smaller than 1 cm and higher than 10 cm are rejected as it is considered that only bubbles of chord length bigger than the separation between probes can be measured accurately, and chord lengths larger than the bed radius would lead to bubble diameters of the order of the column diameter, which are not characteristic of the bubbling regime.
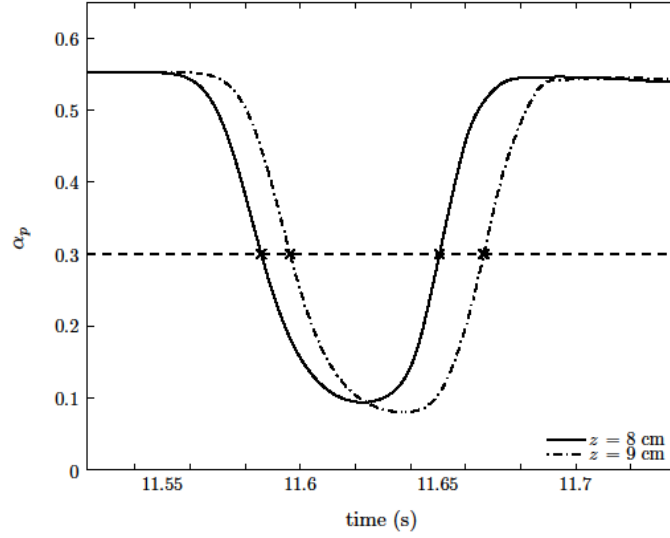
Fig. 5. Example of the computation of the bubble chord length and velocity from solids volume fraction signals for a bubble detected at the bed axis and axial distances z =8 cm and z =9 cm.

3.3 Maximum Entropy Method

The MaxEnt method estimates input probabilities of a process, and in the present paper it is used to reconstruct the distribution of velocity and equivalent volume diameter of bubbles in the simulated fluidized bed as already presented in [26]. The result is a probability distribution that is consistent with known constraints expressed in terms of averages, or expected values, of one or more quantities, but is otherwise as unbiased as possible.

Following the formulation of Sellens and Brzustowski [38], the most appropriate distribution is the function that maximizes the Shannon entropy, which is obtained from the solution of the following problem:

$$P \in \arg\max \int_{x \in \Delta} -P(x) ln(P(x)) dx \qquad (1)$$

subjected to the following i raw moments constraints

$$\int_{x \in \Delta} x^i P(x) dx = \langle x^i \rangle \quad i = 1, \ldots, n \qquad (2)$$

and to the normalization condition

$$\int_{x \in \Delta} P(x) dx = 1 \qquad (3)$$

Where $P(x)$ is the unknown probability density function of the variable x and $\langle x^i \rangle$ is the i-th raw moment of the searched distribution. The raw moments are unknown and, for practical purposes, they are estimated from the measurements or available data.

Following the procedure developed by Rockinger and Jondeau [39], the result of the optimization problem (Eqs. 1-3) can be expressed as:

$$P(x) = \exp\left(\sum_{i=1}^{n} -\lambda_i \left(x^i - \langle x^i \rangle\right)\right) \bigg/ \int_{x \in \Delta} \exp\left(\sum_{i=1}^{n} -\lambda_i \left(x^i - \langle x^i \rangle\right)\right) dx \qquad (4)$$

Where λ_i is the Lagragian multiplier for the i-th moment constraint.

3.3.1 Application to variables from the tomography method

In the case of the tomography method, samples of bubble velocity and equivalent volume diameter are obtained from the tomography reconstruction explained in section (3.1). Then these samples can be directly used to estimate the raw moments. For example, for bubble equivalent volume diameter, raw moments of the sample calculated as $m_i(D_v) = \dfrac{1}{N}\sum_{j}^{N} D_{v,j}^{i}$ can be used to estimate the raw moments $\langle D_v^i \rangle$, where N is the sample size (bubbles counted) and $D_{v,j}$ is the *jth* bubble equivalent volume diameter measured. Then, the maximization problem (Eq. 1-3) is solved obtaining the equivalent volume diameter distribution $P(D_v)$ which is a function that can be expressed as Eq. 4. A schematic diagram of the application of the MaxEnt in this case is shown in Fig.6. The same method applies for the bubble velocity.
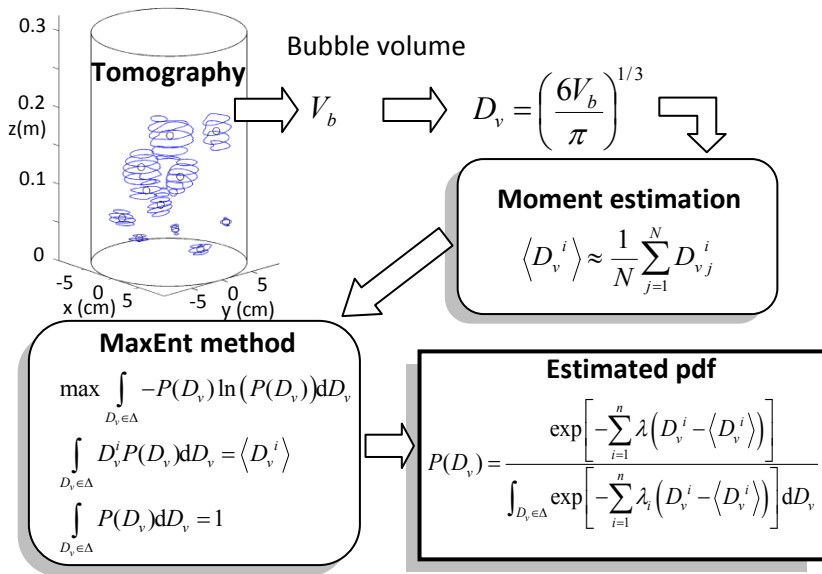
Fig. 6: MaxEnt approach for estimating the distribution of equivalent volume bubble diameter in the tomography method.

3.3.2. Application to variables from the pierced bubble method

The same procedure explained in the previous section can be applied to fit the distribution of bubble vertical velocity extracted from the virtual probes. This is possible because the bubble velocity is a variable that can be directly measured by two voidage probes.

However, in order to obtain the bubble equivalent volume diameter distribution applying the MaxEnt approach, the raw moments of bubble diameter need to be inferred, as diameters cannot be directly measured using virtual voidage probes. In fact, the mayor challenge in the application of the MaxEnt method is to find the required raw moments of the unknowm size distribution from the known raw moments of the chord length distribution.

In this paper, the equivalent volume diameter calculated from the probe signal is obtained assuming truncated oblate spheroid bubbles (with aspect ratio, a, and bubble wake factor Q as indicated in Fig 7) raising vertically, and randomly distributed in a horizontal circular surface containing the probe [20]. In [26], the details of the geometric relationship between chord length and equivalent volume diameter and the derivation of an expression relating the probability density of the bubble equivalent volume diameter, $P(D_v)$ and the raw moments of the sampled chord length, $\langle y^i \rangle$ are given. Using that expression as constraint, the maximization problem to be solved in order to obtain $P(D_v)$ is:

$$P \in \arg\max \int_{D_v \in \Delta} -P(D_v) ln(P(D_v)) dD_v \qquad (5)$$

subjected to the following conditions

$$\int_{D_v \in \Delta} f_i(D_v, s, a, Q, D_v) P(D_v) dD_v = \frac{i+2}{2} \langle y^i \rangle \quad i = 1, \ldots, n \qquad (6)$$

$$\int_{D_v \in \Delta} P(D_v) dD_v = 1 \qquad (7)$$

Where f_i, described in [26], is a function of the equivalent volume bubble diameter, D_v, the distance between probes, s, and the geometrical non-dimensional parameters a and Q of the truncated oblate spheroid. In this expression, the raw moments of the pierced length are estimated from the sample moments of the available data. Moreover, it is considered, as in [26], that only pierced lengths larger than the distance between probes can be measured. In other words, the equivalent volume diameter distribution obtained only accounts for the bubbles that get immersed in both probes while rising.

The maximization problem (Eq. 5-7) can be solved using the method of Lagrange multipliers [38] to give an expression for the distribution $P(D_v)$,

$$P(D_v) = \exp\left(-\lambda_0 - \sum_{i=1}^{n} \lambda_i f_i\right) \qquad (8)$$

Where λ_0 is the Lagragian multiplier for the normalization constraint (Eq. 7) and λ_i is the Lagragian multiplier for the *i-th* moment constraint (Eq. 6). In Fig. 7 a schematic diagram of this procedure is shown.
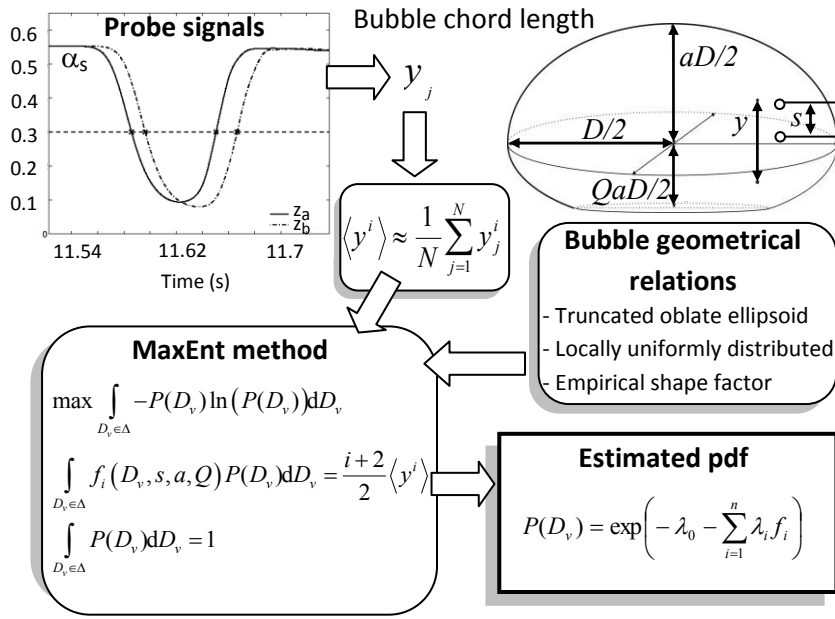
Fig.7. MaxEnt approach for estimating the distribution of equivalent volume bubble diameter in the pierced bubble method.

4. Results and Discussion

As explained in section 3, size and velocity of the bubbles are calculated in this work using two different methods. The pierced bubble method makes use of virtual voidage probes that measure bubble chord lengths and velocities. These signals are processed as described in sections 3.2 and 3.3 to estimate the equivalent volume diameter and velocity distributions. The tomography method uses the whole field of solids volume fraction from which the actual volume and velocity of the simulated bubbles is directly extracted using the tomography reconstruction detailed in section 3.1. The probability density functions of bubble diameter and velocity from both methods are fitted using the MaxEnt method.

4.1. Equivalent volume bubble diameter

The probability density function (pdf) of the equivalent volume bubble diameter calculated using the MaxEnt method is shown in Fig. 8. In particular, Fig. 8a refers to the MaxEnt method applied to the equivalent volume diameters directly obtained from the tomography reconstruction of the bubbles, whereas in Fig. 8b the MaxEnt method was used to fit the distribution of equivalent volume diameters inferred from the chord lengths obtained from virtual probes. Since bubble pierced lengths smaller than 1 cm were discarded and the pierced length is smaller than the diameter of truncated oblate spheroids, the resulting diameters inferred by the MaxEnt method in Fig.8b are larger than 1cm. For the sake of coherence in the comparison, bubbles of diameters less than 1 cm were not considered in the tomography reconstruction. A very similar evolution of the shape of the distributions along the axis of the bed is found for the case of diameters estimated with the chord lengths and the case of

diameters directly obtained with tomography reconstruction. In both cases higher vertical positions in the bed, z, lead to a wider distribution of bubble diameter, D_v. Another similarity is that the most probable value of D_v in the probability density function increases with z in Figs. 8a and 8b. This is in accordance with the growth of bubbles with height because of their coalescence. Also, the modes of the distributions are similar in both cases. However, two distinctions appear between Figs. 8a and 8b. At each distance to the distributor, the probability density function obtained from the tomography reconstruction data (Fig. 8a) shows less probability of finding small bubbles (i.e. close to D_v =1 cm) than the results inferred from the bubble chord lengths (Fig. 8b). This discrepancy between the two probability density functions may be due to the presence of irregularly shaped bubbles that are wrongly viewed as small bubbles with the chord length method. Another difference is that the tail of the distributions at high bubble diameters tends to be more spread out in Fig. 8b than in Fig. 8a. This may be caused by the more restricted conditions in the tomography reconstruction, which neglects big bubbles whenever they start to be connected to the freeboard during eruption. In contrast, information of bubble chord length from two probes of voidage cannot detect in a clear way whether the dome of a bubble is breaking up. As a consequence the distribution functions are flatter for the case of diameters estimated from chord length information.
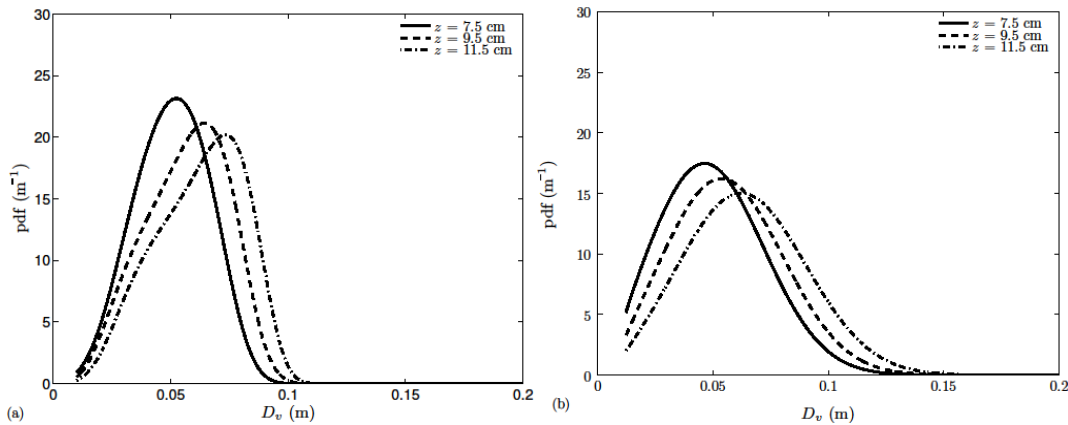
Fig.8. Probability density function of the equivalent volume bubble diameter at three different distances to the distributor: (a) tomography method, (b) pierced bubble method.

The obtained mean values corresponding to the aforementioned distributions of bubble equivalent volume diameter are shown in Fig. 9 along the bed height. The mean bubble diameter increases with height, as already seen in Fig. 8. A very good agreement exists between the diameters estimated from the application of the MaxEnt treatment to the chord lengths and the bubbles directly obtained with tomography reconstruction of the simulated field. Differences between the two results in Fig. 9 are below 4.5%, in the worst case, which suggests that the application of the MaxEnt method to chord lengths can be used with confidence to estimate the bubble diameter in bubbling beds like the one studied here. In Fig. 9, the mean of the chord lengths distributions obtained from the voidage measured by the two virtual probes is also included. According to Karimipour and Pugsley [18] and Rüdisüli et al.[24], the bubble volume (volume average equivalent bubble diameter) can be related to the mean chord length $\langle y \rangle$ by a factor of 1.744. As shown in Fig. 9, application of this conversion factor

provides, in the present case, a very good matching to the directly obtained mean bubble diameter. The maximum discrepancy between $1.744\langle y\rangle$ and the volume directly obtained from tomography is about 5.3%. In Fig. 9 the correlation by Agarwal [40] of bubble size is also represented. The rate of increase of the bubble diameter with distance to the distributor follows fairly well the bubble growth given by the correlation. The difference between the bubble diameter predicted with the correlation and obtained with the simulation reaches 11% in the worst case. Another parameter that describes the probability density functions of Fig. 8 is the standard deviation of the bubble diameter. The standard deviation of diameter is shown in Fig. 10. As expected, the estimations based on MaxEnt applied to chord lengths yield a standard deviation of diameter greater than that for the directly obtained bubbles, since in the former case the distributions are broader than in the latter. This might be due to the fact that the calculation of the bubble size from chord lengths needs to assume a certain bubble shape model, i.e. a truncated oblate spheroid in this case. Although the truncated oblate spheroid represents well the shape of the bubbles in fluidized beds, the tomography method does not require this assumption and it is capable to reconstruct and account for in the bubble size computation the less frequent bubbles of irregular shape.
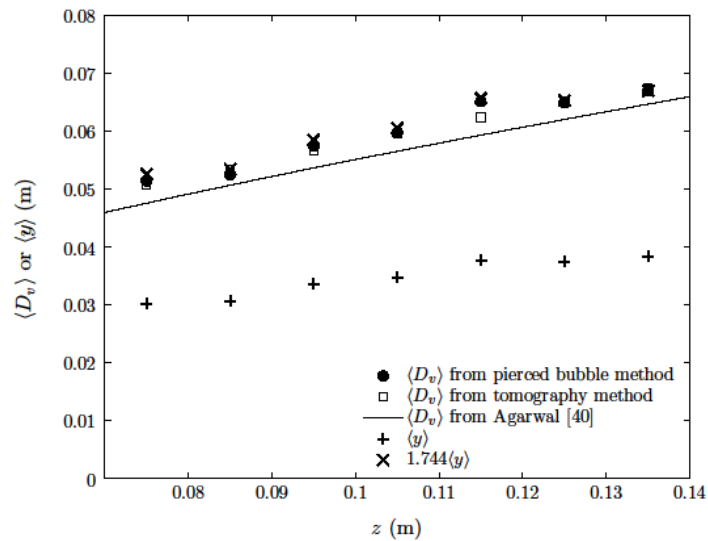
Fig. 9. Comparison of mean values of equivalent volume bubble diameter as a function of the distance to the distributor. Results are obtained with the pierced bubble method, the tomography method and the estimation given by the mean chord length times a conversion factor. The mean value of the sampled chord lengths and the correlation of Argawal [40] are also represented.
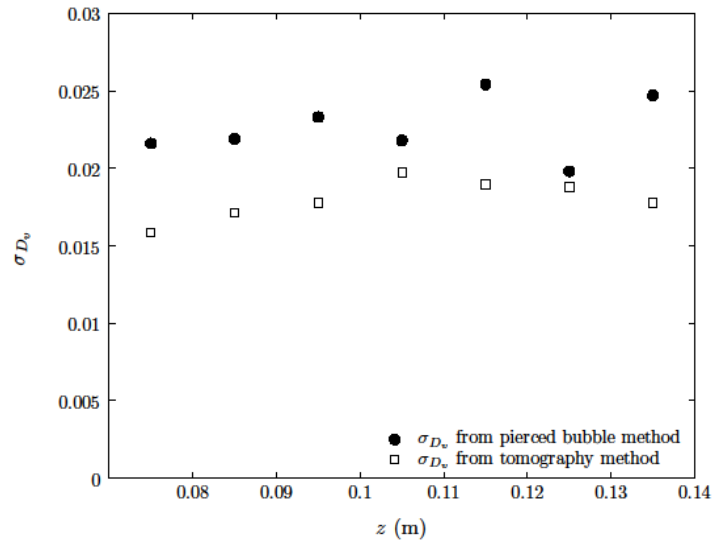
Fig. 10. Comparison of the standard deviations of the equivalent volume bubble diameter obtained with the pierced bubble method and the tomography method as a function of the distance to the distributor.

4.2. Bubble vertical velocity

A comparison of the velocities of the bubbles directly obtained by tomography of the simulated bed and the velocities estimated from the time series of voidage as measured by two virtual probes is presented in Figs. 11 and 12. In particular, the probability density functions of the vertical bubble velocity are compared in Fig. 11 at three different distances to the distributor. As in the case of bubble size, the probability density function of bubble velocities directly obtained from tomography and the probability density function of bubble velocities estimated with the two probes are similar in the sense of shape and predicted values. As expected, increasing the measurement height from the distributor, z, leads to an increase of the most probable value of bubble velocity as bigger bubbles rise faster in the bed. Besides, the density functions spread out for higher heights. The shifting of the probability density function to higher velocities at higher distances to the distributor, i.e. 7.5 cm to 9.5 cm, is very similar for both the tomography and the two probe methods.
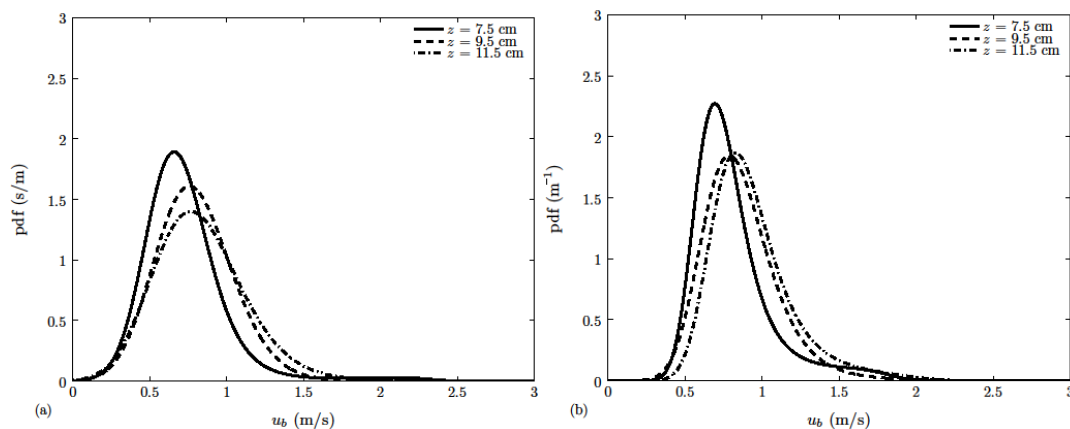
Fig. 11. Probability density function of the vertical bubble velocity at three different distances to the distributor: (a) tomography method, (b) pierced bubble method.

Fig. 12 shows the mean of the bubble velocity distributions of Fig. 11 as a function of the height from the distributor. In Fig.12 the bubble velocity obtained as in [23] using the classical correlation proposed by Davidson and Harrison [41] is also shown. The tomography results are in very good agreement with the correlation, and differences are in the order of 10%. The similarity of the bubble velocity directly obtained from tomography and the estimation using the time series of voidage from two virtual probes is in general satisfactory. In the two cases, the mean bubble velocity tends to increase with height, z . This is in good agreement with the expected increase in velocity due to the growth of bubbles (see Fig. 9) while they rise in the bed. In Fig. 12, results of bubble velocity progress with z more smoothly when calculated with the two probes than those directly obtained from the tomography of the whole field. This can be explained considering that results obtained from the virtual probes are typically a filtered reflection of what is actually happening in the bed, owing to the less sensitivity of these two probe measurements on bubble deformation and coalescence. The relative difference between the estimation of bubble velocity using two virtual probes and the more exact bubble velocity directly obtained with tomography is about 17% in the worst case. As seen in Fig. 12, the use of two virtual probes of voidage yields bubble velocities that are greater than the bubble velocity obtained with tomography. Additionally, Fig. 13 shows that the standard deviation of the bubble velocity is similar for the two methods, as expected from the comparable shape of the distributions shown in Fig. 11. Inspection of Fig. 11 indicates that these comparatively large values of the mean of velocity are promoted by the longer tails of the distribution functions obtained with two probe measurements. As noted before, the spread out of the tails towards larger velocities in the probability density function calculated with two probes may be related to the presence of large bubbles not taken into account during their break-up by the tomography reconstruction.
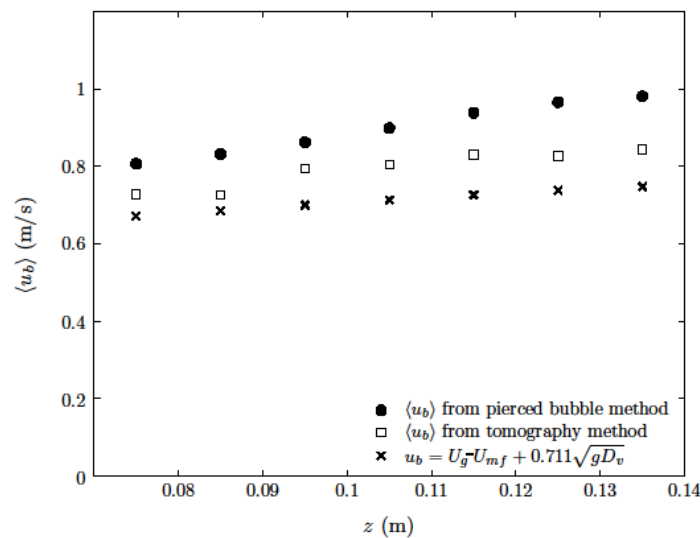
Fig. 12. Comparison of mean values of bubble velocity obtained with the pierced bubble method and the tomography method as a function of the distance to the distributor. The correlation of Davidson and Harrison [41] is also presented.
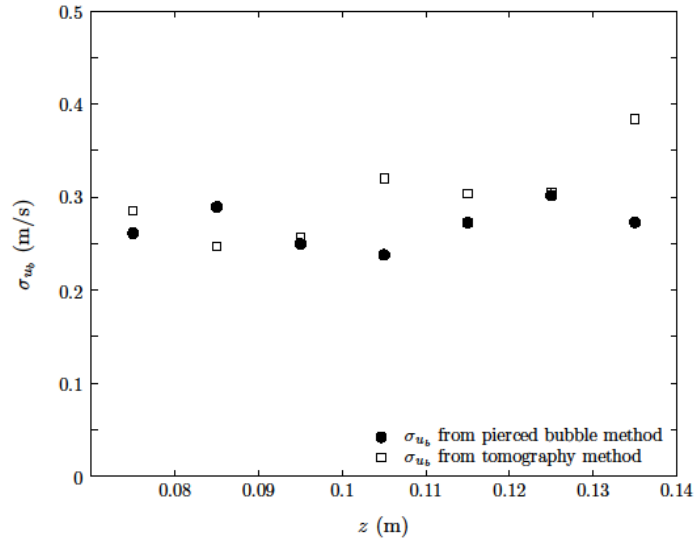

Fig.13. Comparison of the standard deviation of bubble velocity obtained with the pierced bubble method and the tomography method as a function of the distance to the distributor.

5. Conclusions

3D dense phase fields that are fully resolved in space and time, resulting from the simulation of a cylindrical bed column, were employed in the present work to directly extract the volume-based diameter and velocity of bubbles in the interior of the cylindrical bed. The technique proposed for this direct extraction was a tomography reconstruction of the instantaneous 3D field. The results were compared with the bubble diameter and velocity calculated from the signals of two virtual probes of voidage immersed in the simulated bed. The bubble diameter from the virtual probes was estimated with the MaxEnt method applied to the sampled values of the bubble chord lengths. This comparison indicated that the mean bubble diameter can be confidently estimated with the MaxEnt approach and two probe signals. The differences between the bubble diameter so estimated and that obtained with the more accurate tomography reconstruction are less than 4.5% for the studied bed. Concerning the mean bubble velocity, the estimation using the pierced bubble method tends to overpredict the vertical velocity of bubbles compared to the velocity directly obtained with tomography, though differences were not greater than 17%. For the bubble diameter and velocity, it was found that the probability density function estimated from the pierced bubble method and the probability density function obtained with tomography method were similar in general terms. For example, they coincide in reproducing the growth of the most probable value and the spread out of the distribution functions of bubble size and velocity when the distance to the distributor increases. The detected differences may be caused by complex phenomena like bubble deformation, coalescence and break-up, which are not fully detected by two probe measurements of voidage.

Nomenclature

a	aspect ratio of the truncated oblate spheroid
C_D	drag coefficient
d_p	particle diameter (m)
D_v	equivalent volume bubble diameter (m)
e_{pp}	restitution coefficient
g	gravity acceleration (m/s^2)
$g_{0,pp}$	radial distribution function
H	column height (m)
h_o	bed settled height (m)
$\boldsymbol{I}$	unit tensor
I_{2D}	second invariant of the deviatory stress tensor
k_Θ	diffusion coefficient of granular temperature (kg/ms)
K_{gp}	gas-particle momentum exchange coefficient (kg/m^{3}s)
N_i	number of iterations per time step
P	probability density function
p	pressure (Pa)
Q	bubble wake factor of the truncated oblate spheroid
R	column radius (m)
Re	Reynolds number
s	distance between probes (m)
t	time (s)
u_b	bubble velocity (m/s)
U_g	superficial gas velocity (m/s)
U_{mf}	minimum fluidization velocity (m/s)
V_b	Bubble volume (m^3)
$\boldsymbol{v}$	velocity vector (m/s)

y	bubble chord length (m)
$\langle y \rangle$	mean value of y (m)
z	vertical distance to the distributor (m)

Greek letters

α	volume fraction
ϕ	angle of internal friction
γ_Θ	collision dissipation energy (kg/ms^3)
λ	bulk viscosity (Pa s)
μ	shear viscosity (Pa s)
Θ	granular temperature (m^2/s^2)
ρ	density (kg/m^3)
σ	standard deviation
τ	shear stress tensor (Pa)
Ψ	tracking coefficient

Subscripts

g	gas phase
max	maximum value
p	particulate phase
th	threshold

References

[1] D. Kunii, O. Levenspiel, Fluidization Engineering, Butterworth-Heinemann, Newton, MA, 1991.

[2] L. Shen, F. Johnsson, B. Leckner, Digital image analysis of hydrodynamics two-dimensional bubbling fluidized beds. Chem. Eng. Sci. 59 (2004) 2607-2617.

[3] J.A. Laverman, I. Roghair, M. van Sint Annaland, H. Kuipers, Investigation into the hydrodynamics of gas-solid fluidized beds using particle image velocimetry coupled with digital image analysis. Can. J. Chem. Eng., 86 (2008) 523-535.

[4] A. Busciglio, V. Giuseppa, G. Micale, L. Rizzuti, Analysis of the bubbling behavior of 2D gas solid fluidized beds Part I. Digital image analysis technique, Chem. Eng. J. 140 (2008) 398-413.

[5] A. Busciglio, V. Giuseppa, G. Micale, L. Rizzuti, Analysis of the bubbling behavior of 2D gas solid fluidized beds Part II. Comparison between experiments and numerical simulations via Digital image analysis technique, Chem. Eng. J. 148 (2008) 145-163.

[6] T. Li, J.R. Grace, X. Bi, Study of wall boundary condition in numerical simulations of bubbling fluidized beds. Powder Technol. 203 (2010) 447-457.

[7] F. Hernández-Jiménez, S. Sánchez-Delgado, A. Gómez-García, A. Acosta-Iborra, Comparison between two-fluid model simulations and particle image analysis & velocimetry (PIV) results for a two-dimensional gas-solid fluidized bed. Chem. Eng. Sci., 66 (2011) 3753-3772.

[8] F. Hernández-Jiménez, J.R. Third, A. Acosta-Iborra, C.R. Müller, Comparison of bubble eruption models with two-fluid simulations in a 2D gas-fluidized bed. Chem. Eng. J., 171 (2011) 328-339.

[9] E. Cano-Pleite, F. Hernández-Jiménez, M. de Vega, A. Acosta-Iborra, Experimental study on the motion of isolated bubbles in a vertically vibrated fluidized bed. Chem. Eng. J. 255 (2014) 114-125.

[10] D.J. Patil, M. van Sint Annaland, J.A.M Kuipers, Critical comparison of hydrodynamic models for gas–solid fluidized beds—part I: bubbling gas–solid fluidized beds operated with a jet. Chem. Eng. Sci. 60 (2005) 57–72.

[11] I. Hulme, E. Clavell, L. van der Lee, A. Kantzas, CFD modeling and validation of bubble properties for a bubbling fluidized bed. Ind. Eng. Chem. Res. 44 (2005) 4254–4266.

[12] V. Verma, J.T. Padding, N.G. Deen, J.A.M. Kuipers, Bubble formation at a central orifice in a gas-solid fluidized bed predicted by three-dimensional two-fluid model simulations. Chem. Eng. J. 245 (2014) 217-227.

[13] J.M. Weber, J.S. Mei, Bubbling fluidized bed characterization using Electrical Capacitance volume Tomography (ECVT). Powder Technol. 242 (2013) 40-50.

[14] R.F. Mudde, Time-resolved X-ray tomography of a fluidized bed. Powder Technol. 199 (2010) 55-59.

[15] J.B. Drake, T.J. Heindel, Local time-average gas holdup comparisons in cold flow fluidized beds with side-air injection. Chem. Eng. Sci. 68 (2012) 157-165.

[16] K. Dubrawski, S. Tebianan, H.T. Bi, J. Chaouki, N. Ellis, R. Gerspacher, R. Jafari, A. Kantzas, C. Lim, G.S. Patience, T. Pugsley, M.Z. Qi, J.X. Zhu, J.R. Grace, Traveling column for comparison of invasive and non-invasive fluidization voidage measurement techniques. Powder Technol. 235 (2013) 203-220.

[17] C. Rautenbach, R.F. Mudde, X. Yang, M.C. Melaaen, B.M. Halvorsen, A comparative study between electrical capacitance tomography and time-resolved X-ray tomography. Flow Meas. Instrum. 30 (2013) 34-44.

[18] S. Karimipour, T. Pugsley, A critical evaluation of literature correlations for predicting bubble size and velocity in gas-solid fluidized beds. Powder Technol. 205 (2011) 1-14.

[19] G.C. Brouver, E.C. Wagner, J.R. van Ommen, R.F. Mudde, Effects of pressure and fines content on bubble diameter in a fluidized bed studied using fast X-ray tomography. Chem. Eng. J., 207-208 (2012) 711-717.

[20] J. Werther, Bubbles in gas fluidized beds –Part I. Trans. Instn. Chem. Engrs, 52 (1974) 149-159.

[21] C. Sobrino, A. Acosta-Iborra, D. Santana, M. de Vega, Bubble characteristics in a bubbling fluidized bed with a rotating distributor. Int. J. Multiphase flow 35 (2009) 970-976.

[22] M. Liu, Y. Zhang, H. Bi, J.R. Grace, Y. Zhu, Non-intrusive determination of bubble size in gas-solid fluidized bed: an evaluation. Chem. Eng. Sci. 65 (2010) 3485-3493.

[23] M. Rüdisüli, T.J. Schildhauer, S.M.A Biollaz, J.R. van Ommen, Bubble characterization in a fluidized bed by means of optical probes. Int. J. Multiphase flow 41 (2012) 56-67.

[24] M. Rüdisüli, T.J. Schildhauer, S.M.A Biollaz, J.R. van Ommen, Monte Carlo simulation of the bubble size distribution in a fluidized bed with intrusive probes. Int. J. Multiphase flow 44 (2012) 1-14.

[25] D. Santana, J. Rodríguez-Rodríguez, J.A. Almendros-Ibáñez, C. Martínez-Bazán, Characteristic lengths and maximum entropy estimation from probe signals in the ellipsoidal bubble regime. Int. J. Multiphase Flow 32 (2006) 1123-1139.

[26] C. Sobrino, J.A. Almendros-Ibáñez, D. Santana, C. Vázquez, M. de Vega, M., Maximum entropy estimation of the bubble size distribution in fluidized beds. Chem. Eng. Sci. 64 (2009) 2307-2319.

[27] A. Acosta-Iborra, C. Sobrino, F. Hernández-Jiménez, M. de Vega, Experimental and computational study on the bubble behavior in a 3-D fluidized bed. Chem. Eng. Sci. 66 (2011) 3499–3512.

[28] V. Verma, N.G. Deen, J.T. Padding, J.A.M. Kuipers, Two-fluid modeling of three-dimensional cylindrical gas-solid fluidized beds using the kinetic theory of granular flow. Chem. Eng. Sci. 102 (2013) 227-245.

[29] F. Meng, N. Zhang, W. Wang, Virtual experimentation of beam hardening effect in X-ray CT measurement of multiphase flow. Powder Technol. 194 (2009) 153-157.

[30] B.G.M. van Wachem, A.E. Almstedt, Methods for multiphase computational fluid dynamics, Chem. Eng. J. 96 (2003) 81-98.

[31] D. Gidaspow, Multiphase Flow and Fluidization, Academic Press, Boston, 1994.

[32] D. Gidaspow, R. Bezburuah, J. Ding, J., Hydrodynamics of circulating fluidized beds, kinetic theory approach, in: Fluidization VII, Proceedings of the 7th Engineering Foundation Conference on Fluidization, 1992, pp. 75–82.

[33] C.K.K. Lun, S.B. Savage, D.J. Jeffrey, N. Chepurniy, Kinetic Theories for Granular Flow: Inelastic Particles in Couette Flow and Slightly Inelastic Particles in a General Flow Field, J. Fluid Mech. 140 (1984) 223-256.

[34] D.G. Schaeffer, Instability in the Evolution Equations Describing Incompressible Granular Flow, J. Differ. Equations 66 (1987) 19-50.

[35] S.V. Patankar, Numerical Heat Transfer and Fluid Flow, Taylor & Francis, Levittown, 1998.

[36] B.R. Hutchinson, G.D. Raithby, A Multigrid Method Based on the Additive Correction Strategy. Numer. Heat Transfer 9 (1986) 511-537.

[37] M.J.V. Goldschmidt, J.A.M. Kuipers, W.P.M. van Swaaij, Hydrodynamic modelling of dense gas-fluidised beds using the kinetic theory of granular flow: effect of coefficient of restitution on bed dynamics. Chem. Eng. Sci. 56 (2001) 571-578.

[38] R.W. Sellens, T.A. Brzustowski, A simplified prediction of droplet velocity distributions in a spray. Combust. Flame 65 (1986) 273–279.

[39] M. Rockinger, E. Jondeau, Entropy densities with an application to autoregressive conditional skewness and kurtosis. J. Econometrics 106 (2002) 119-142.

[40] P.K. Agarwal, Bubble characteristics in gas-fluized beds. Chem. Eng. Res. Des. 63 (1985), 323-337.

[41] J.F. Davidson and D. Harrison, Fluidized Particles, first ed., Cambridge University Press, Cambridge, New York, 1963.

Figure captions

Fig. 1. Schematic representation of the simulated fluidized bed including the boundary conditions and virtual probes location.

Fig. 2. Snapshots of isocontours for α_p=0.3 showing the 3D bubbles obtained from the two-fluid simulation at three sequential time instants.

Fig.3. Tomographic identification and reconstruction of bubbles: (a) determination of sectioned bubble contours by horizontally sectioning the simulated field of solids volume fraction in the bed and (b) reconstruction of 3D bubbles by matching and pilling up the sectioned bubble contours. The small circle in each bubble denotes its centroid.

Fig. 4. Solids volume fraction at the bed axis and axial distance z =8 cm (a) and z =9 cm (b). The solids volume fraction threshold $\alpha_{p,th}$ =0.3 is indicated with a dashed line and bubbles detected are marked with a circle.

Fig. 5. Example of the computation of the bubble chord length and velocity from solids volume fraction signals for a bubble detected at the bed axis and axial distances z =8 cm and z =9 cm.

Fig. 6: MaxEnt approach for estimating the distribution of equivalent volume bubble diameter in the tomography method.

Fig.7. MaxEnt approach for estimating the distribution of equivalent volume bubble diameter in the pierced bubble method.

Fig.8. Probability density function of the equivalent volume bubble diameter at three different distances to the distributor: (a) tomography method, (b) pierced bubble method.

Fig. 9. Comparison of mean values of equivalent volume bubble diameter as a function of the distance to the distributor. Results are obtained with the pierced bubble method, the tomography method and the estimation given by the mean chord length times a conversion factor. The mean value of the sampled chord lengths and the correlation of Argawal [40] are also represented.

Fig. 10. Comparison of the standard deviations of the equivalent volume bubble diameter obtained with the pierced bubble method and the tomography method as a function of the distance to the distributor.

Fig. 11. Probability density function of the vertical bubble velocity at three different distances to the distributor: (a) tomography method, (b) pierced bubble method.

Fig. 12. Comparison of mean values of bubble velocity obtained with the pierced bubble method and the tomography method as a function of the distance to the distributor. The correlation of Davidson and Harrison [41] is also presented.

Fig.13. Comparison of the standard deviation of bubble velocity obtained with the pierced bubble method and the tomography method as a function of the distance to the distributor.

Table

Table 1 Main geometrical and operational characteristics of the fluidized bed.

Parameter	Value	Parameter	Value
R (m)	0.0965	ρ_p (kg/m^3]	2632.5
H (m)	0.8	ρ_g [kg/m^3]	1.225
h_0 (m)	0.22	μ_g [Pa·s]	1.789e-5
d_p (μm)	540	U_g [m/s]	0.57

Table

Table 2 Governing equations of the two-fluid model.

Mass conservation equations

$$\frac{\partial}{\partial t}\left(\alpha_g \rho_g\right) + \nabla \cdot \left(\alpha_g \rho_g \mathbf{v}_g\right) = 0 \tag{T2-1}$$

$$\frac{\partial}{\partial t}\left(\alpha_p \rho_p\right) + \nabla \cdot \left(\alpha_p \rho_p \mathbf{v}_p\right) = 0 \tag{T2-2}$$

Momentum conservation equations

$$\frac{\partial}{\partial t}\left(\alpha_g \rho_g \mathbf{v}_g\right) + \nabla \cdot \left(\alpha_g \rho_g \mathbf{v}_g \mathbf{v}_g\right) = -\alpha_g \nabla p + \nabla \cdot \left(\alpha_g \boldsymbol{\tau_g}\right) - K_{gp}(\mathbf{v}_g - \mathbf{v}_p) + \alpha_g \rho_g \mathbf{g} \tag{T2-3}$$

$$\frac{\partial}{\partial t}\left(\alpha_p \rho_p \mathbf{v}_p\right) + \nabla \cdot \left(\alpha_p \rho_p \mathbf{v}_p \mathbf{v}_p\right) = -\alpha_p \nabla p - \nabla p_p + \nabla \cdot \left(\alpha_p \boldsymbol{\tau}_p\right) + K_{gp}(\mathbf{v}_g - \mathbf{v}_p) + \alpha_p \rho_p \mathbf{g} \tag{T2-4}$$

Granular temperature equation

$$\frac{3}{2}\left[\frac{\partial}{\partial t}\left(\rho_p \alpha_p \Theta\right) + \nabla \cdot \left(\rho_p \alpha_p \Theta \mathbf{v_p}\right)\right] = \left(-p_p \mathbf{I} + \boldsymbol{\tau}_p\right) : \nabla \mathbf{v_p} + \nabla \cdot \left(k_\Theta \nabla \cdot \Theta\right) - \gamma_\Theta - 3K_{gp}\Theta \tag{T2-5}$$

Table 3 Closure models selected for the simulation of the fluidized bed.

A.- Coefficient of drag between gas and particles [31]:

$$K_{gp} = \frac{3}{4} C_D \frac{\alpha_p \alpha_g \rho_g |\mathbf{v}_p - \mathbf{v}_g|}{d_p} \alpha_g^{-2.65} \quad \text{for } \alpha_g > 0.8 \tag{T3-1}$$

$$K_{gp} = 150 \frac{\alpha_p^2 \mu_g}{\alpha_g d_p^2} + 1.75 \frac{\alpha_g \rho_g |\mathbf{v}_p - \mathbf{v}_g|}{d_p} \quad \text{for } \alpha_g \leq 0.8 \tag{T3-2}$$

Where the drag coefficient is defined as:

$$C_D = \frac{24}{\alpha_g \, \mathrm{Re}_p} \left[1 + 0.15 \left(\alpha_g \, \mathrm{Re}_p \right)^{0.687} \right] \tag{T3-3}$$

With $\mathrm{Re}_p = \dfrac{\rho_g d_p |\mathbf{v}_p - \mathbf{v}_g|}{\mu_g}$ \hfill (T3-4)

B.- Solids pressure [32]:

$$p_p = \alpha_p \rho_p \Theta + 2\rho_p (1 + e_{pp}) \alpha_p^2 g_{0,pp} \Theta \tag{T3-5}$$

Where the radial distribution function is:

$$g_{0,pp} = \left[1 - \left(\frac{\alpha_p}{\alpha_{p,\max}} \right)^{1/3} \right]^{-1} \tag{T3-6}$$

C.- Solids stress tensor:

$$\boldsymbol{\tau}_p = \alpha_p \mu_p \left(\nabla \mathbf{v}_p + \nabla \mathbf{v}_p^{\mathrm{T}} \right) + \alpha_p \left(\lambda_p - \frac{2}{3} \mu_p \right) \nabla \cdot \mathbf{v}_p \, \mathbf{I} \tag{T3-7}$$

Where solid bulk viscosity is [32]:

$$\lambda_p = \frac{4}{3}\alpha_p \rho_p d_p g_{0,pp}(1+e_{pp})\left(\frac{\Theta}{\pi}\right)^{1/2}$$

(T3-8)

and solid shear viscosity is

$$\mu_p = \mu_{p,col} + \mu_{p,fr} + \mu_{p,kin}$$

(T3-9)

which is composed of a kinetic viscosity [31]

$$\mu_{p,kin} = \frac{10\rho_p d_p \sqrt{\Theta\pi}}{96\alpha_p(1+e_{pp})g_{0pp}}\left[1+\frac{4}{5}g_{0pp}\alpha_p(1+e_{pp})\right]^2$$

(T3-10)

a collisional viscosity [31]

$$\mu_{p,col} = \frac{4}{5}\alpha_p \rho_p d_p g_{0,pp}(1+e_{pp})\left(\frac{\Theta}{\pi}\right)^{1/2}$$

(T3-11)

and a frictional viscosity [33]

$$\mu_{p,fr} = \frac{p_p \sin\phi}{2\sqrt{I_{2D}}}$$

(T3-12)

where ϕ is the angle of internal friction, and I_{2D} is the second invariant of the deviatory stress tensor.

D.- Diffusion coefficient of granular temperature [31]:

$$k_\Theta = \frac{150\rho_p d_p \sqrt{\Theta\pi}}{384\left(1+e_{pp}\right)g_{0pp}}\left[1+\frac{6}{5}\alpha_p g_{0pp}\left(1+e_{pp}\right)\right]^2$$

$$+2\rho_p d_p \alpha_p^{\,2} g_{0pp}\left(1+e_{pp}\right)\sqrt{\frac{\Theta}{\pi}}$$

(T3-13)

E.- Collisional dissipation of energy [32]:

$$\gamma_\Theta = \frac{12(1-e_{pp}^{\,2})g_{0,pp}}{d_p\sqrt{\pi}}\rho_p \alpha_p^{\,2}\Theta^{3/2}$$

(T3-14)

Table

Table 4 Main parameters selected for the simulation.

Parameter	Value	Parameter	Value
e_{pp} [ ]	0.9	g [m/s^2]	9.81
$\alpha_{p,\max}$ [ ]	0.555	Δt [s]	2.5e-4
ϕ [degree]	30	N_i	40

Figure

Top:

Pressure outlet

1 atm

Walls:

No-slip condition for air

Zero particle-wall shear stresses

Bubbles

Measurement points

Distributor:

Uniform velocity inlet

p_o

R

H

h_0

z

p_8
p_7
p_6
p_5
p_4
p_3
p_2
p_1

Fluidized bed

Air U_g
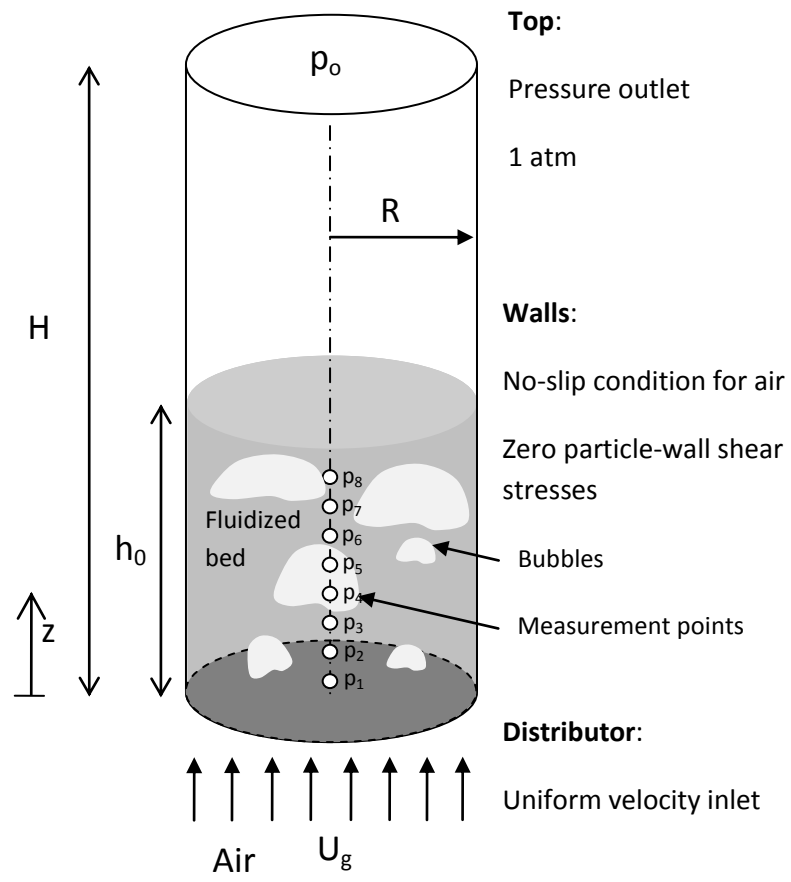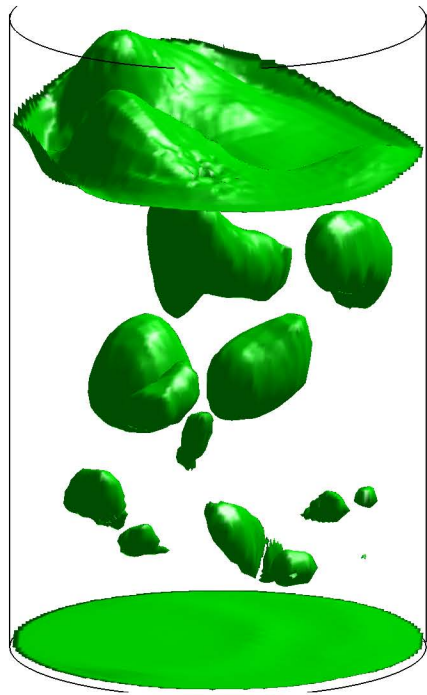
Figure

$t_1 = 47.676$ s $t_2 = t_1 + 100\Delta t$ $t_3 = t_1 + 200\Delta t$

(a)

(b)

(a)

time (s)

(b)

time (s)

Figure

Figure

(a)

Figure

(b)

Figure

Figure

(a)

Figure

(b)
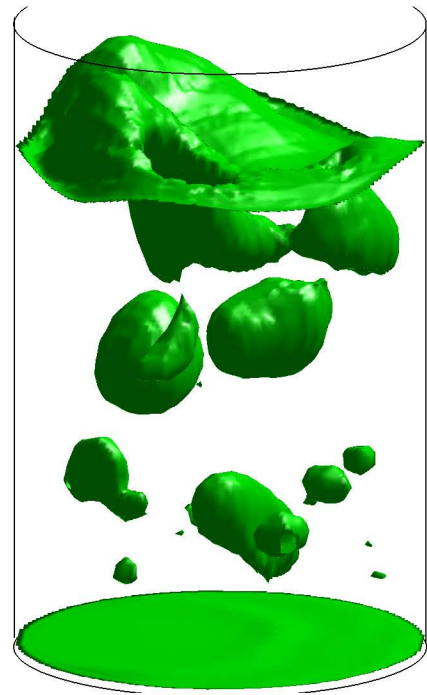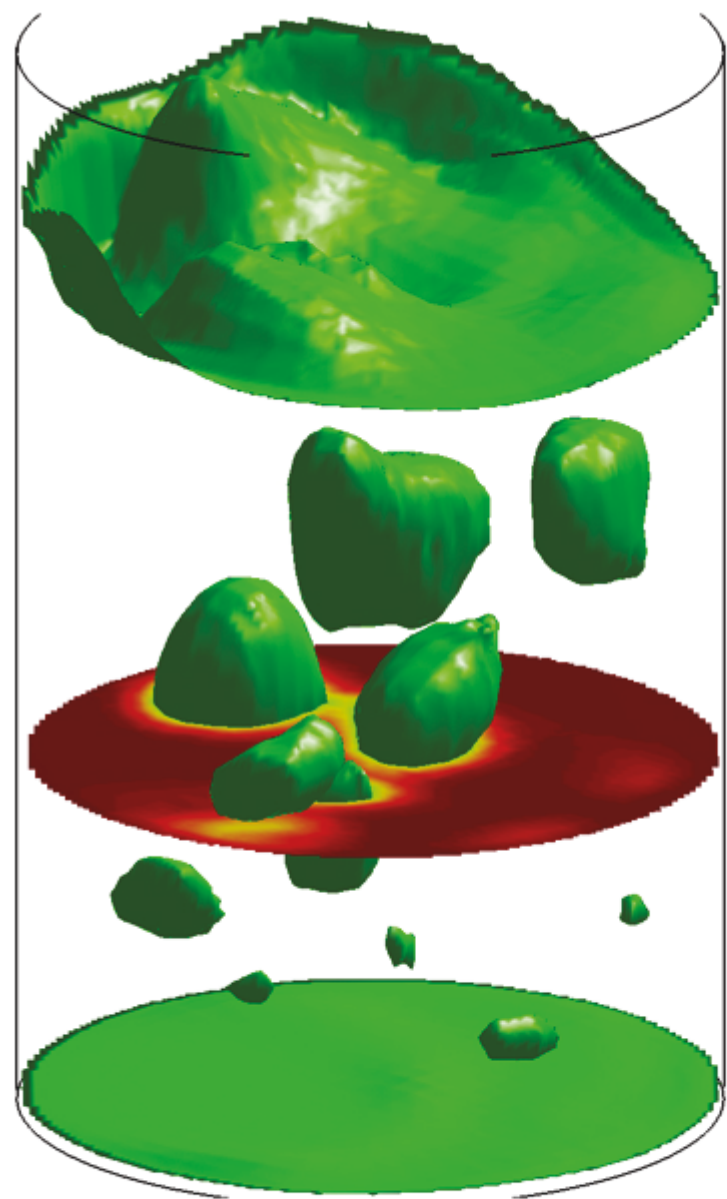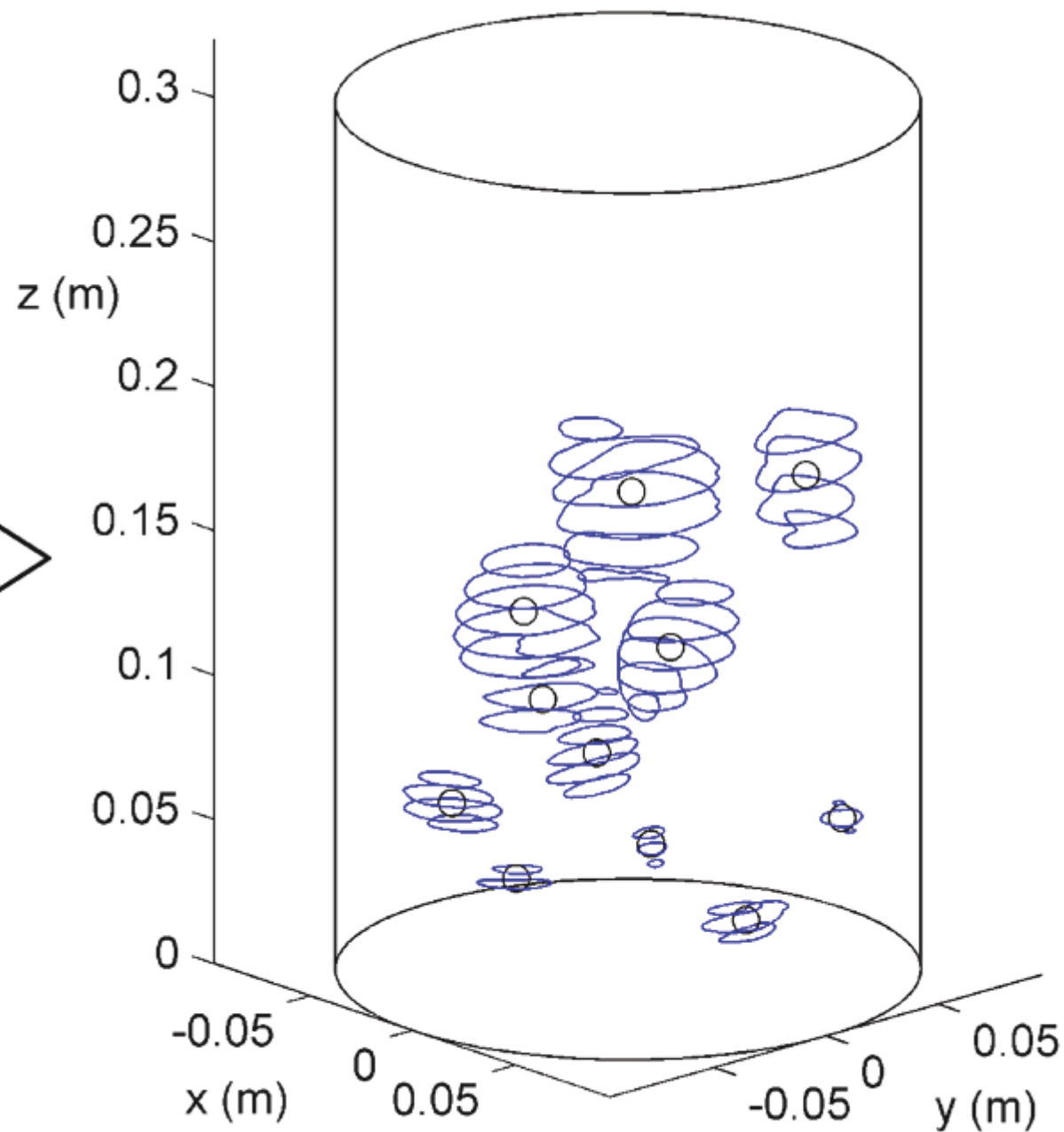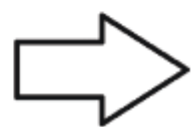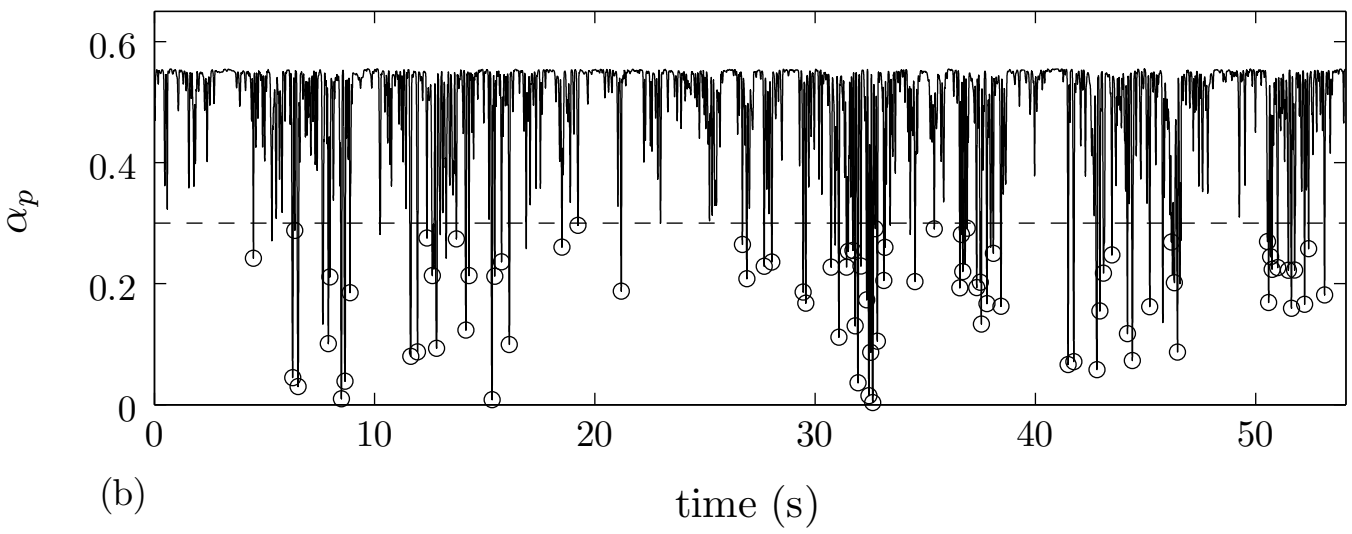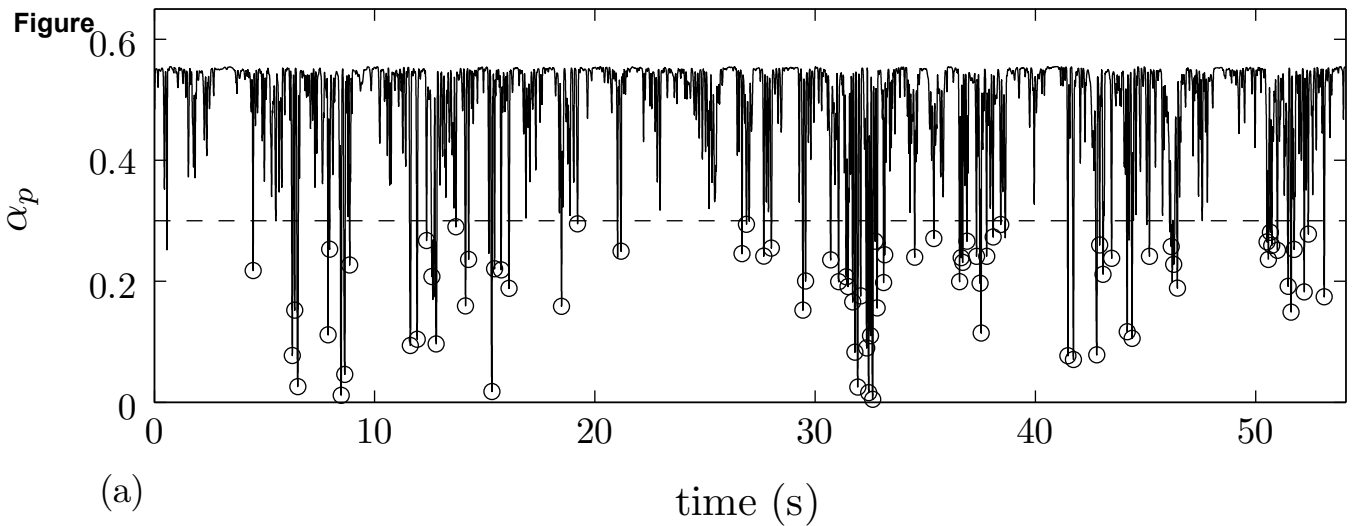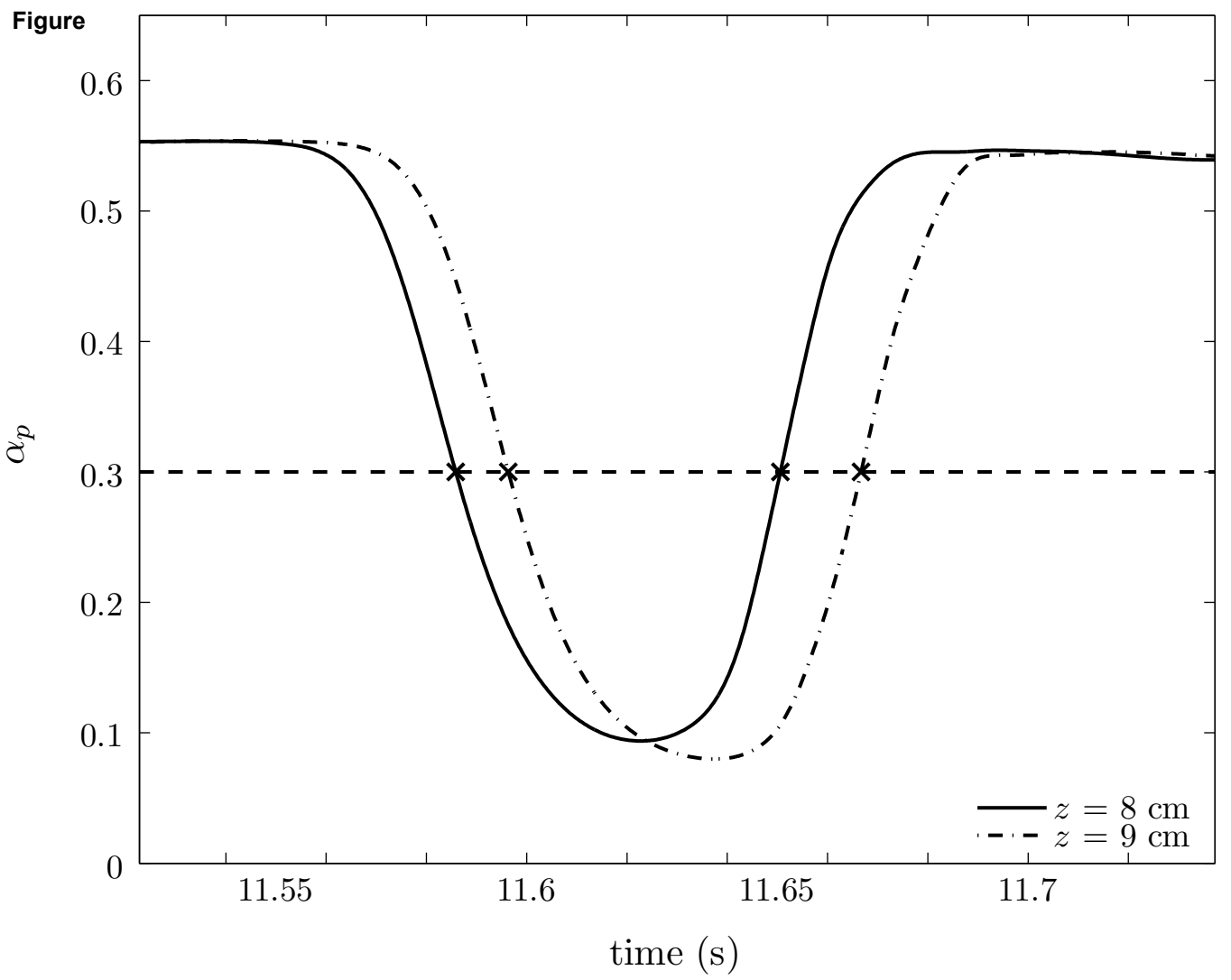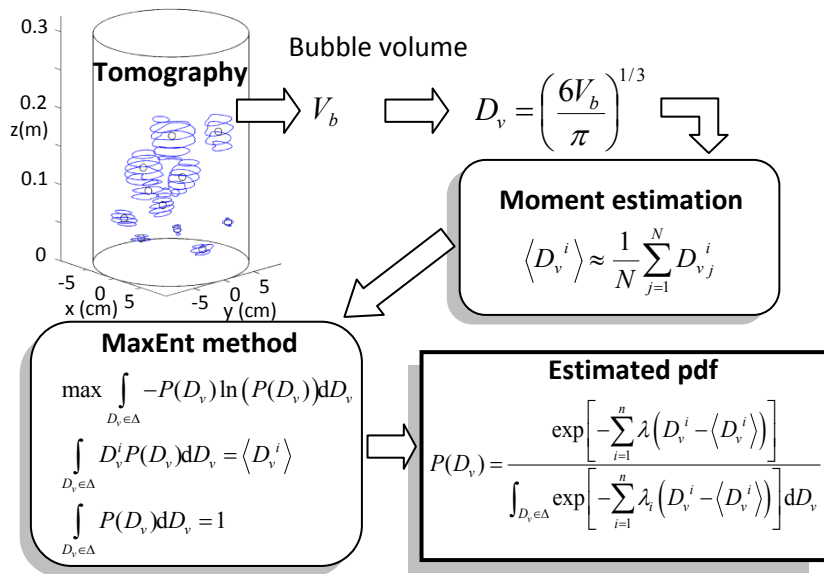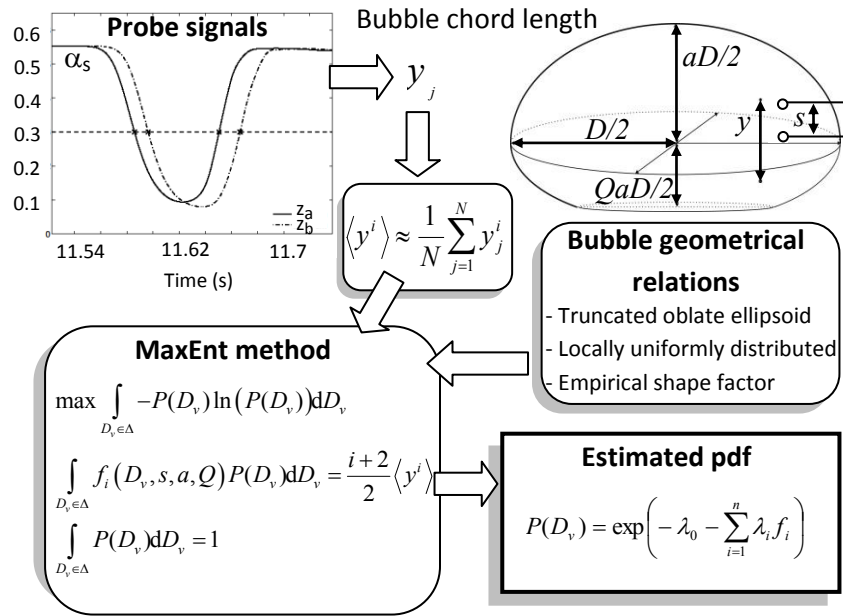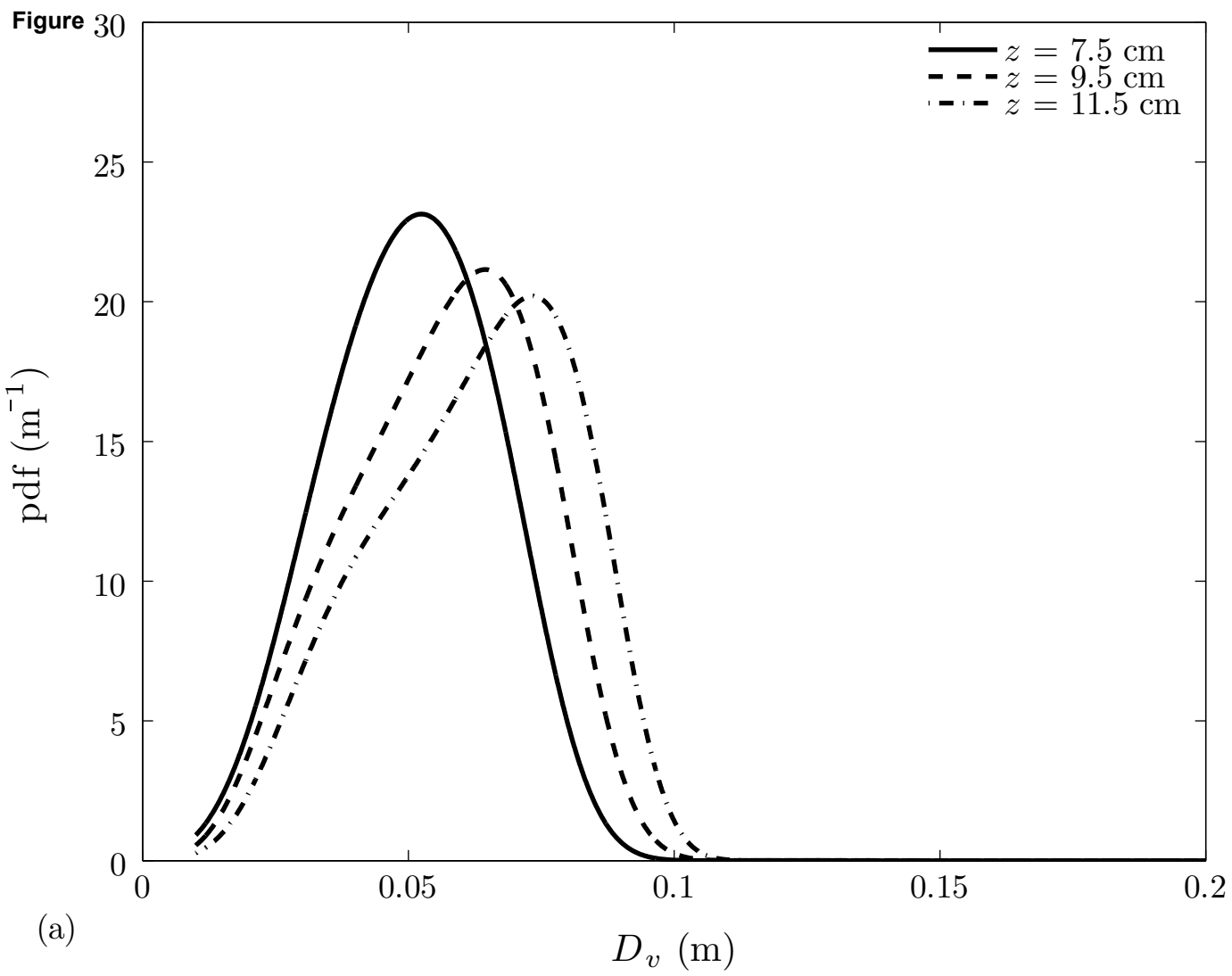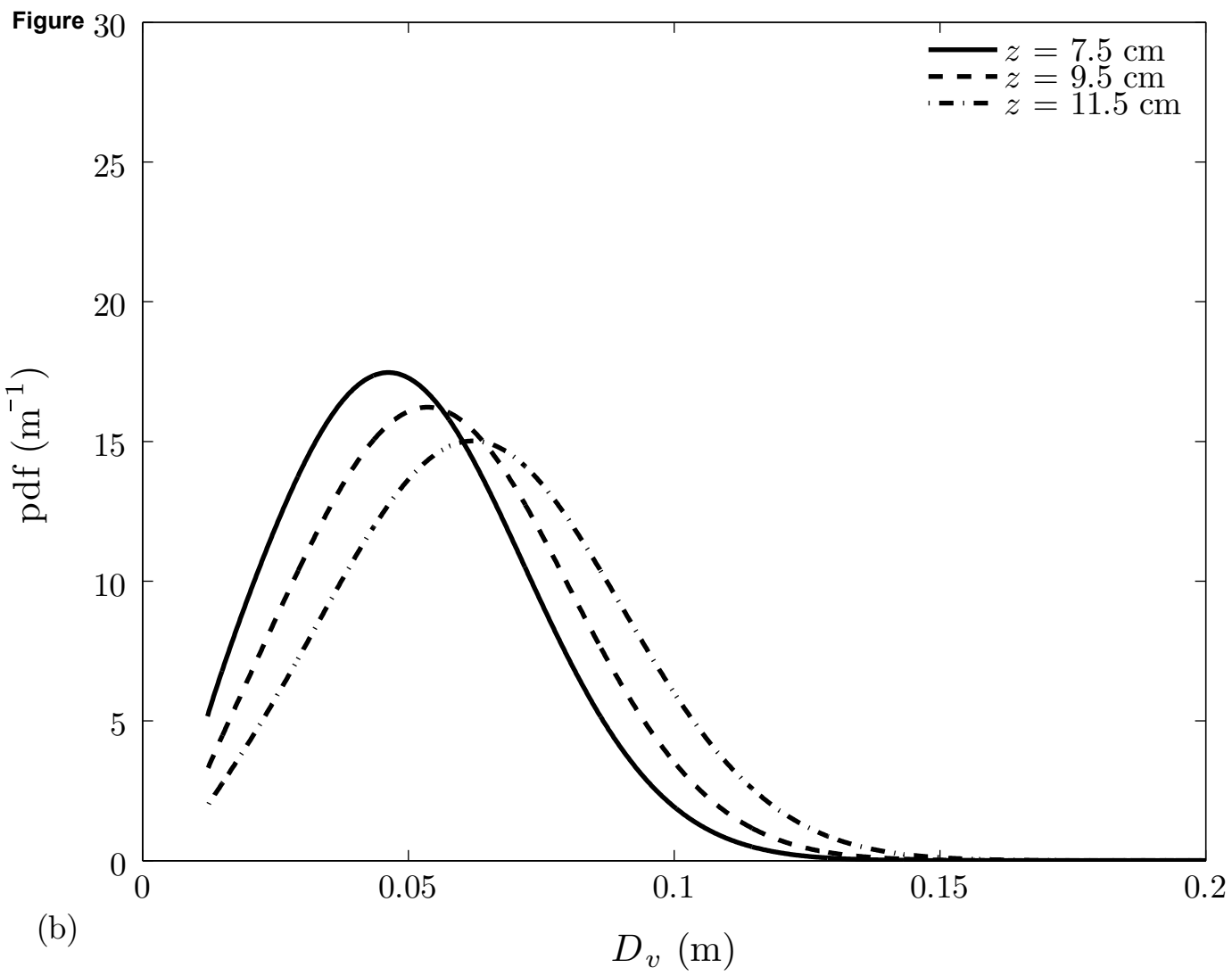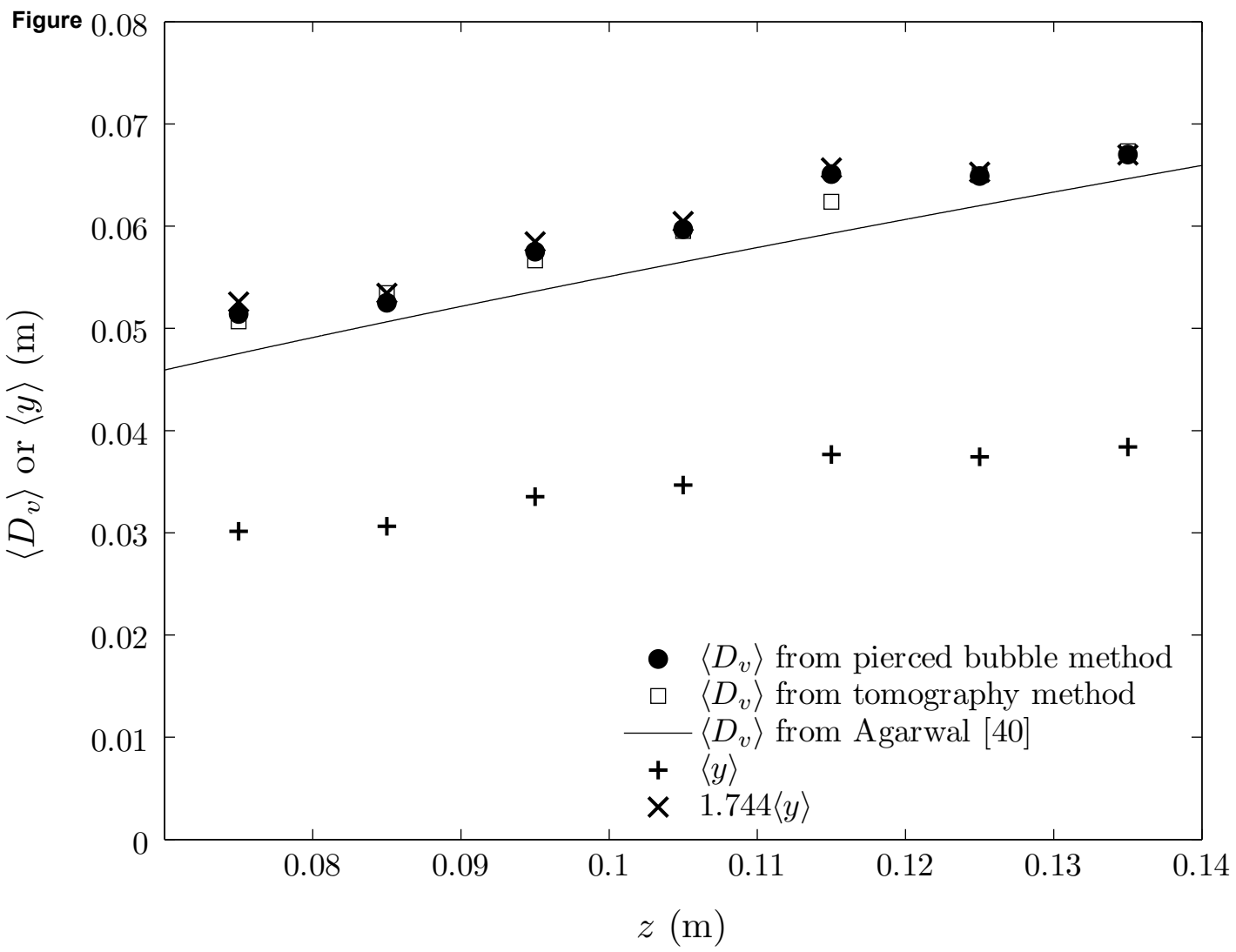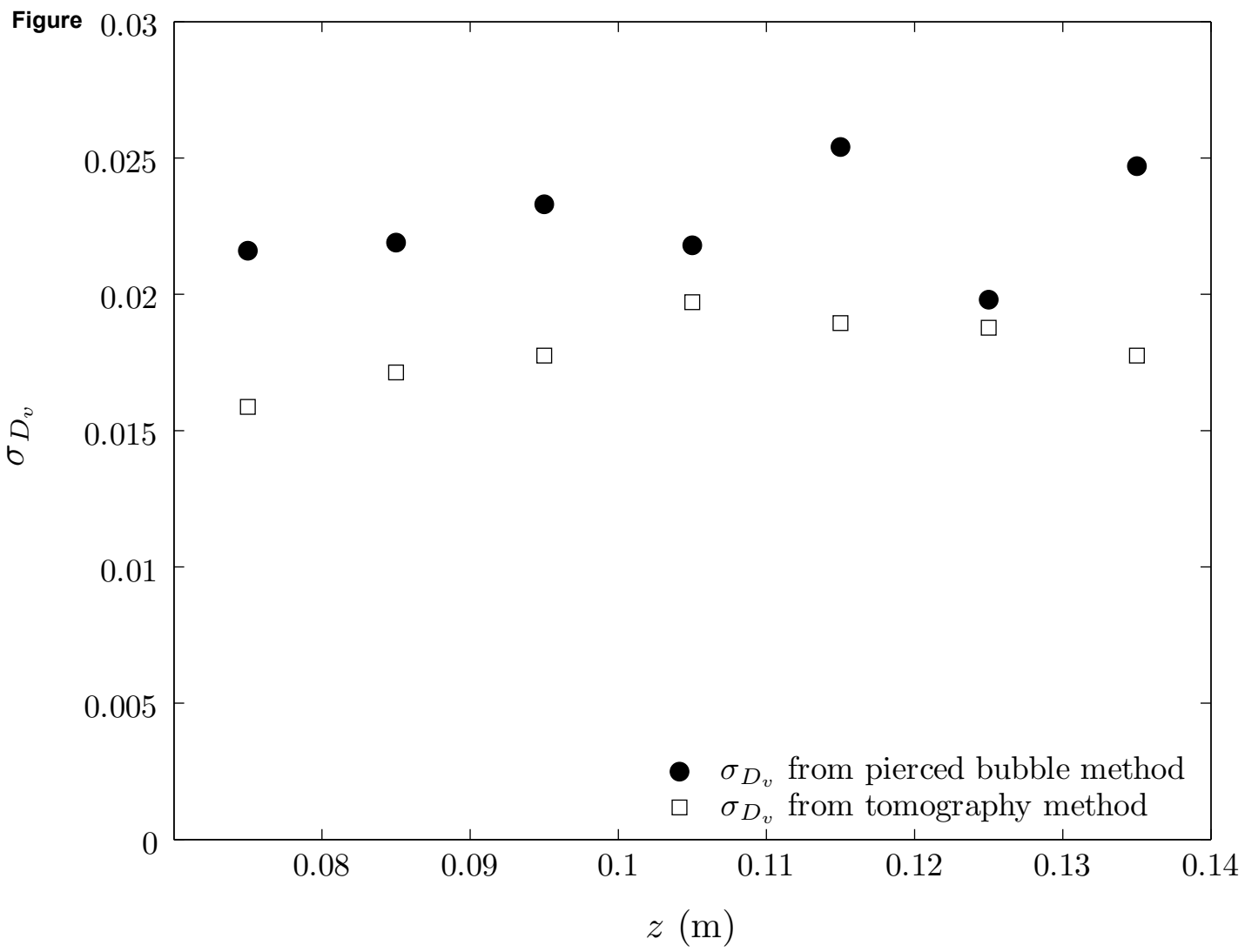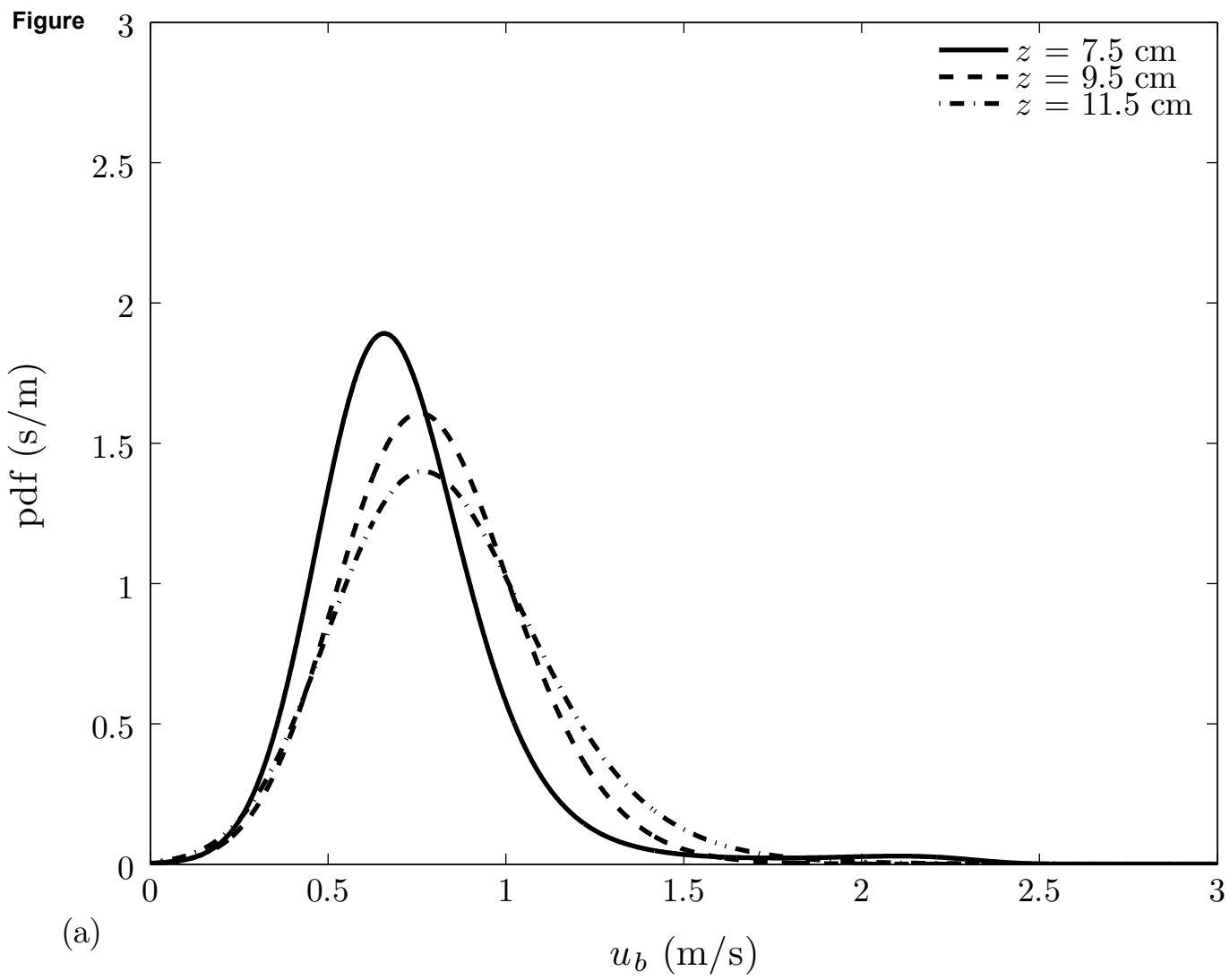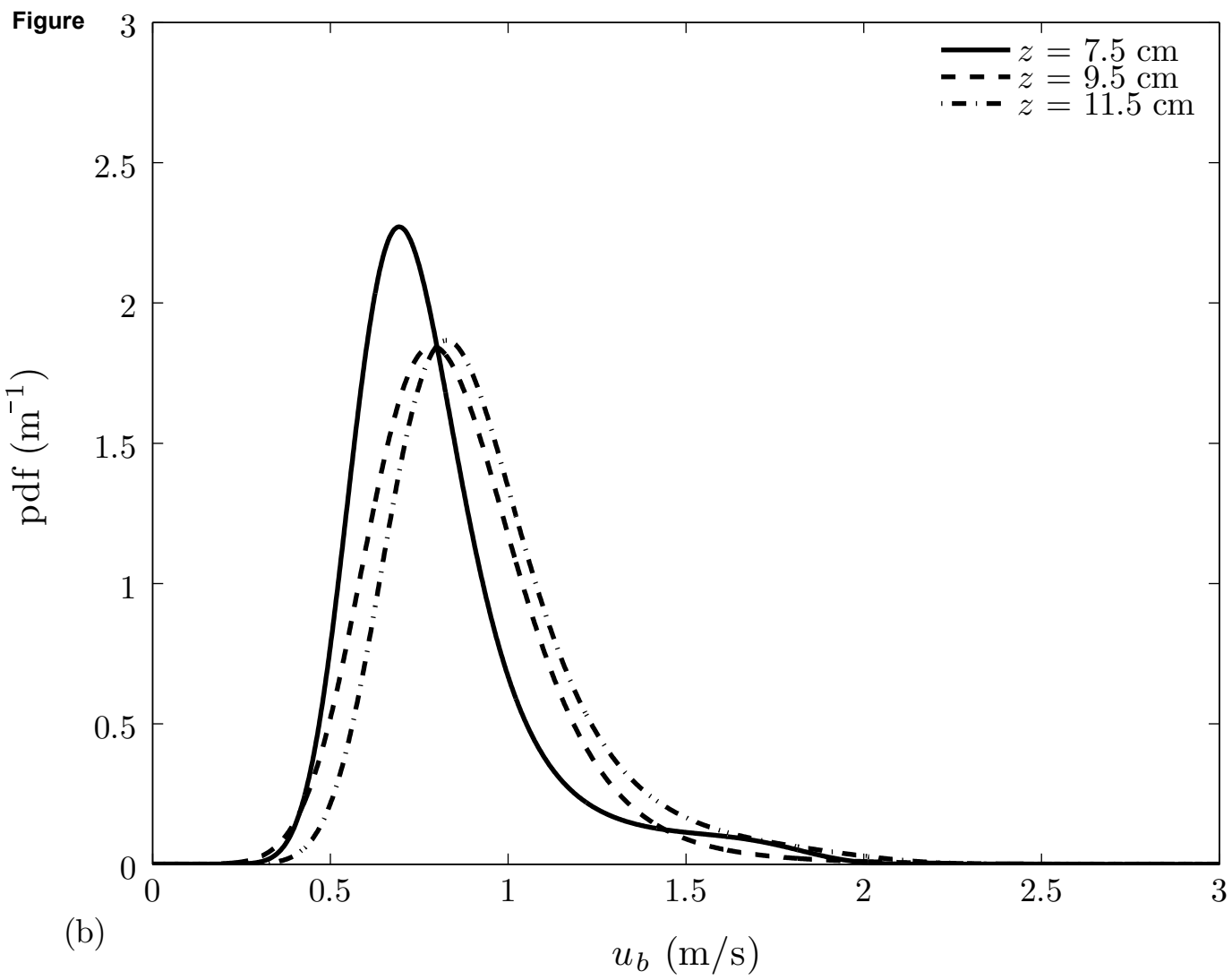
Figure

Figure

Supplementary MATLAB .fig files

Supplementary MATLAB .fig files

Click here to download Supplementary MATLAB .fig files: Fig5.fig

Supplementary MATLAB .fig files

Supplementary MATLAB .fig files

Supplementary MATLAB .fig files

Supplementary MATLAB .fig files

Click here to download Supplementary MATLAB .fig files: Fig10.fig

Supplementary MATLAB .fig files

Supplementary MATLAB .fig files

Supplementary MATLAB .fig files

Supplementary MATLAB .fig files

Click here to download Supplementary MATLAB .fig files: Fig13.fig